






## Article

# A “Zero-Cost” Adsorbing Hydroxyapatite-Based Material from Amazon Fishery Waste for Water Remediation and Nutrient Release for Agriculture

Carmen Greice Renda <sup>1,2</sup>, Thamara Machado de Oliveira Ruellas <sup>1,2,\*</sup> , João Otávio Donizette Malafatti <sup>2</sup> ,  
Carla Suellem Sousa Araújo <sup>3</sup>, Gabriela Leite da Silva <sup>1,2</sup> , Bruno Apolo Miranda Figueira <sup>3</sup>, Simone Quaranta <sup>4</sup>   
and Elaine Cristina Paris <sup>2</sup> 

<sup>1</sup> Federal University of São Carlos, Washington Luís Highway, 235 km–SP 310, São Carlos 13565-905, SP, Brazil

<sup>2</sup> Nanotechnology National Laboratory for Agriculture (LNNA), Embrapa Instrumentação, XV de Novembro Street, 1452, São Carlos 13560-970, SP, Brazil

<sup>3</sup> Federal University of Pará West (UFOPA), Vera Paz Street, Tapajós Unit, Pará 68040-255, PA, Brazil

<sup>4</sup> Institute of Nanostructured Materials (ISMN)–Italian National Research Council (CNR), Strada Provinciale 35 d, n. 9, Montelibretti, 00010 Rome, RM, Italy

\* Correspondence: thamararuellas@gmail.com

**Abstract:** This paper puts forward the use of “low-cost/low-end” hydroxyapatite-based adsorbing materials prepared from Tambaqui fish cleaning residues (i.e., bones) by grinding and/or thermal annealing. The nature of raw materials and treatments practically resulted in a “zero-cost” adsorbent for atrazine pesticide and Co<sup>2+</sup> ion remediation in an aqueous solution. Despite the distinctive character of the two contaminants, all adsorptions were found to follow pseudo-second order kinetics and Freundlich isotherm models. Pristine hydroxyapatite proved to be more effective in adsorbing atrazine at low concentrations due to interactions with collagen residues. Conversely, heat-treated materials demonstrated better adsorption performances for cobalt due to the removal of organic residues hindering access to the surface. On the other hand, lower adsorption affinities resulted into a faster and more efficient Co<sup>2+</sup> release into water. The different behavior in terms of phosphate and cobalt release shown by the three hydroxyapatite-based adsorbents can be exploited for differential liberation of targeted nutrients, with high seed germination rates. Considering circular economic principles, waste-derived hydroxyapatites may be potentially attractive for removing ionic species, minimizing water pollution stemming from heavy industry, and for their subsequent targeted release to edible plants, enhancing agricultural availability of mineral nutrients for soil fertilization.

**Keywords:** hydroxyapatite; water remediation; amazon region; fish cleaning waste; atrazine; cobalt; plant nutrition; circular economy



**Citation:** Renda, C.G.; Ruellas, T.M.d.O.; Malafatti, J.O.D.; Araújo, C.S.S.; Silva, G.L.d.; Figueira, B.A.M.; Quaranta, S.; Paris, E.C. A “Zero-Cost” Adsorbing Hydroxyapatite-Based Material from Amazon Fishery Waste for Water Remediation and Nutrient Release for Agriculture. *Physchem* **2023**, *3*, 34–60. <https://doi.org/10.3390/physchem3010004>

Academic Editor: Francesco Mallamace

Received: 16 November 2022

Revised: 21 December 2022

Accepted: 28 December 2022

Published: 1 January 2023



**Copyright:** © 2023 by the authors. Licensee MDPI, Basel, Switzerland. This article is an open access article distributed under the terms and conditions of the Creative Commons Attribution (CC BY) license (<https://creativecommons.org/licenses/by/4.0/>).

## 1. Introduction

Human activities have been impacting the global environment since the Industrial Revolution [1]. Among the diverse kinds of pollutants, a great deal of attention has been devoted to water reservoir and waste-water contamination by inorganic and organic compounds stemming from industrial manufacturing and agriculture. Certain water pollutants (e.g., agrochemicals, antibiotics) are recalcitrant to conventional combined mechanical/microbiological treatments. Therefore, research studies have been wide and continuously conducted using diverse and multifunctional materials, aiming at multi-focused environmental remediation (e.g., adsorbents from activated charcoal [2–7], alumina [8–11], clays [12–14], resins [15,16], silica [17,18], zeolites [19–22], and metal–organic frameworks [23–27], among others). Adsorption remains a staple of any waste-water treatment [28], with fast and usually inexpensive processes, accessible to developing countries [29]. In addition, adsorbents can be tailored to the pollutant and made recoverable and

reusable by devising proper supporting materials. Finally, adsorption usually generates no environmentally harmful byproducts [30–32].

Hydroxyapatite (HAp,  $\text{Ca}_{10}(\text{PO}_4)_6(\text{OH})_2$ ) is a naturally occurring mineral encountered in mammal bones (i.e., bone mineral) and teeth. Because of its non-toxic nature, HAp has been adopted in applications where biocompatibility and high chemical and thermal stability are crucial factors, such as bone tissue engineering, edentulous ridge augmentation, and orthopedic and dental implant coatings. Concerning adsorption processes, HAp has been evaluated for capture and controlled release of a wide spectrum of bioactive chemical species (e.g., antibiotics, anti-cancer agents, proteins, radionuclides, and genetic material) [33–36]. Moreover, HAp has been investigated extensively as an adsorbent for various pollutants such as dyes [37], herbicides [38], and heavy metals [39–41].

Preparation of HAp materials matching environmental remediation requirements has been relying on either chemical synthesis employing commercial precursors or extraction from natural sources. Synthetic methods include co-precipitation [42], sol-gel, sonochemical, ultrasound microwave, calcination, alkaline hydrolysis, hydrothermal, or combined approaches. A vast number of natural sources have been explored as starting materials to extract HAp [43–45]. As opposed to the numerous synthetic routes, alkaline hydrolysis, hydrothermal treatment, and calcination are regarded as the only relevant techniques to extract HAp from a series of biological sources or wastes, such as mammalian bones (e.g., bovine, camel, and horse), marine or aquatic sources (e.g., fish bone and fish scale), shell materials (e.g., cockle, clam, eggshell, and seashell), plants, algae, and also from mineral sources (e.g., limestone) [46–48]. According to the U.N. Food and Agricultural Organization (FAO), about 25% of material resulting from fish-related industries (e.g., fishery, pisciculture, and canning) is discarded as waste [49,50]. Hence, a conspicuous quantity of “zero”-cost materials is potentially available every year for the extraction of natural, mostly non-stoichiometric hydroxyapatite [51]. As for Brazil, a fish known as Tambaqui (*Colossoma macropomum*) has dominated fishing and fish farming for the last few years [52,53]. Indeed, total Tambaqui production amounted to 262,370 tons, corresponding to a 31.2% share of the Brazilian domestic fish market, in 2019. Naturally, synthesizing value-added materials from fish bones and scales is considered a valuable option to reduce pollution associated to fish cleaning waste [54].

Pesticides are widespread agrochemicals used in agriculture to prevent the proliferation of plagues. Nevertheless, they also represent a significant source of waterway contamination. According to the latest pesticide commercialization report issued by the Brazilian Institute for the Environment and Natural Resources (Instituto Brasileiro de Meio Ambiente e dos Recursos Naturais–IBAMA), Brazil marketed 685,746.68 tons of agrochemicals in 2020, which represents a 10.51% increase in domestic sales compared to 2019 [55,56]. Specifically, atrazine (a herbicide) is the fourth most commercialized pesticide (33,321 tons in 2020) [57,58].

Regarding environmental concerns, pollution caused by commonly occurring inorganic ions, especially in watercourses, has been a research focus as much as pesticides [59,60]. Among heavy metals, cobalt (Co) is one of the most controversial with respect to the effects on human health. Excessive exposure to cobalt can induce adverse human health effects in terms of neurological (i.e., hearing and visual impairment), cardiovascular, and endocrine deficits [61,62]. On the other hand,  $\text{Co}^{2+}$  is a necessary component of vitamin B<sub>12</sub> (hydroxocobalamin) and an essential coenzyme for cell mitosis [63,64]. Aside from being fundamental for animal metabolism, cobalt has recently been recognized as a potentially essential nutrient for plants [65–67]. For instance, the  $\text{Co}^{2+}$  is indispensable to leguminous plants because of its role in nitrogen (N) fixation by symbiotic microbes [66]. Indeed, vitamin B<sub>12</sub> is required by several enzymes responsible for N<sub>2</sub> fixation. Even within the symbiosis domain, cobalt is critical (along with molybdenum and vanadium) for a group of nitrogen-fixing bacteria known as diazotrophs [68–72].

The present paper proposes a strategy for capturing and re-utilizing inorganic and organic pollutants predicated on a low-cost adsorbent. Specifically, HAp-based adsorbents were fabricated from a “zero-cost” source of hydroxyapatite (Tambaqui fish bones) by simple heat treatment procedures. Atrazine (ATZ) and cobalt ( $\text{Co}^{2+}$ ) were the targeted contaminants to be removed from aqueous solutions. The effect of different annealing temperatures on the raw material and their impact on the adsorbent properties were evaluated. Furthermore, liberation of micro- $(\text{Co}^{2+})$  and macro- $(\text{PO}_4^{3-})$  nutrients from the HAp adsorbents turned out to be beneficial for plant seed germination. Thus, considering a circular economy and environmental sustainability, HAp from fish cleaning waste may represent a “low-end” platform for environmental remediation capable of joining adsorption of potentially harmful contaminants as a novel approach on the slow release of micronutrients for agricultural use.

## 2. Materials and Methods

### 2.1. Preparation of Hydroxyapatite-Based Adsorbents (F-HAp, HAp<sub>600</sub> °C, and HAp<sub>900</sub> °C)

Tambaqui (*Colossoma macropomum*) cleaning waste was collected from different local fish markets in Santarem, Pará, Brazil. Fish residues were boiled briefly to separate the organic part from the inorganic one. Afterward, the fish bones were washed and dried at room temperature for 48 h. A mortar was used to homogenize the pristine adsorbent that was labeled as fish-hydroxyapatite (F-HAp). This raw material was conditioned in porcelain crucibles and heat treated at two different temperatures: 600 °C for 2 h (HAp<sub>600</sub> °C), and 900 °C for 2 h (HAp<sub>900</sub> °C), in a Jung® (Schalksmühle, Germany) Furnace coupled to a Novus® (Canoas, Brazil) N1200 controller at a 10 °C min<sup>-1</sup> heating rate. The three HAp-based materials were characterized and evaluated for adsorption of organic (atrazine) and inorganic (cobalt) pollutants in aqueous solutions. The costs associated with all hydroxyapatite-based materials were considered virtually zero, and thus they were denominated as low-cost/zero-cost materials. This is justified by the consideration that the source of expense is derived only from the cost of the two-hour furnace heat treatment step, which is variable according to the specifications of the furnace employed and the local kWh price. The F-HAp material has no such cost (non-heat-treated raw sample).

### 2.2. Characterizations

A field emission gun scanning electron microscopy (FEG-SEM) 6700 JEOL® (Tokyo, Japan) equipment operating at 7 kV was used for the morphological characterization of the samples (particle size, shape, and distribution). The zeta potential (ZP) and dynamic light scattering (DLS) measurements were performed with a Malvern® (Malvern, United Kingdom) Zetasizer NanoSZ to gain a deeper insight into particle stability and size.

The crystallinity of the adsorbents before and after thermal treatment was estimated by X-ray diffraction through a Lab-XRD-6000 Shimadzu® (Kyoto, Japan) diffractometer equipped with a Cu-K $\alpha$  radiation source ( $\lambda = 1.5406 \text{ \AA}$ ),  $2\theta$  angular range from 5° to 80°, and a scanning step of 1° min<sup>-1</sup>. Crystalline phases were assigned with a 95% reliability (Crystallographica search-match [73]), and the unit cell parameters were determined by the least squares refinement (UnitCell [74]). The full width at half maximum (FWHM) measurement was obtained from the nonlinear Lorentzian fit of the peak. Structural models were rendered from sample and reference diffractogram data, together with cell parameters, using a three-dimensional structure visualization program (VESTA [75]).

Chemical bond information and additional structural features were attained by Fourier Transform Infrared (FT-IR) spectroscopy in ATR mode performed with a Vertex 70 Bruker® (Karlsruhe, Germany) spectrophotometer (spectral range 400–4000 cm<sup>-1</sup>).

Thermogravimetric analysis (TG) was employed to verify the thermal stability of the adsorbents and the elimination temperature of organic molecules, collagen, and water. TG was conducted with a TA Instruments® (New Castle, United States of America) SDT650 equipment, in a platinum pan, under 40 mL min<sup>-1</sup> nitrogen flux and 60 mL min<sup>-1</sup> air flux, from room temperature to 900 °C.

### 2.3. Pollutants: Atrazine Adsorption Experiments

As for adsorption evaluation, 1.00 g L<sup>-1</sup> atrazine (ATZ) stock aqueous solution (Sigma-Aldrich®, St. Louis, United States of America, 99%) was prepared by first dissolving the herbicide in a minimum amount of methanol (Êxodo Científica®, Sumaré, Brazil, 99.8%). Adsorbent samples were weighed and placed in 15 mL falcon tubes filled with the target solution and stirred in a powder shaker at 100 rpm at room temperature (30 °C). Samples were centrifuged at 8000 rpm for 10 min before contaminant concentration measurements. Several experimental parameters were varied to optimize adsorption conditions, including contact time (kinetic study) and initial contaminant concentration (adsorption isotherms). Kinetic studies were performed with 0.01 g of HAp in 10 mL of an atrazine solution (10 mg L<sup>-1</sup>). Different sampling times (5, 10, 15, 30, 60, 120, 240, 1440, 2880, and 4320 min) were used. Adsorption isotherm studies were conducted with 10 mg of HAp in 10 mL of eight different ATZ diluted aqueous solutions (5, 10, 25, 50, 100, 125, 150, and 200 g L<sup>-1</sup>). All adsorption tests were replicated three times. Atrazine solutions were centrifuged to recover the adsorbent and analyze the supernatant by UV-Vis spectrophotometry (Shimadzu®, Kyoto, Japan, 1600 equipment) in order to quantify the amount of AZT adsorbed by HAp. Spectroscopical data were deconvoluted (multiple peak fit analysis based on Gaussian curves) to identify the isolated contributions of the atrazine peaks.

Adsorption capacities ( $q$ , mg g<sup>-1</sup>) at equilibrium and/or at a given time were determined using the mass balance condition given by Equation (1):

$$q = \frac{(C_0 - C)V}{m} \quad (1)$$

where  $C_0$  is the initial contaminant concentration (mg L<sup>-1</sup>);  $C$  is the concentration (mg L<sup>-1</sup>) of adsorbate at equilibrium and/or at a given time;  $V$  is the solution volume (L); and  $m$  is the mass of adsorbent (g).

Kinetic experimental data were fitted with pseudo-first and pseudo-second order models, whereas Langmuir and Freundlich were models used to study the adsorbent-adsorbate interaction in terms of adsorption isotherms. The linear equations employed in the kinetic and isotherm studies are given in Table 1 by Equations (2)–(6), along with the initial adsorption rate determination, which is given by Equation (4).

**Table 1.** Linear forms of kinetic and isotherm models.

Model	Equations	Linear Form	References
Pseudo-first order kinetics	(2)	$\log(q_{eq} - q_t) = \log q_{eq} - \frac{k_{1st}}{2.303} t$	[76]
Pseudo-second order kinetics	(3)	$\frac{t}{q_t} = \frac{1}{k_{2nd} q_{eq}^2} + \frac{1}{q_{eq}} t$	[77]
	(4)	$h_0 = k_{2nd} q_{eq}^2$	[78]
Langmuir Isotherm	(5)	$\frac{C_{eq}}{q_{eq}} = \frac{1}{q_{max}} C_{eq} + \frac{1}{K_{Lg} q_{max}}$	[79]
Freundlich Isotherm	(6)	$\log q_{eq} = \log K_{Fr} + \frac{1}{n} \log C_{eq}$	[80]



#### 2.4. Pollutants: Cobalt Adsorption and Release Experiments

Cobalt adsorption tests were similarly performed. Briefly, a 50 mg L<sup>-1</sup> stock solution of Co<sup>2+</sup> ions (CoCl<sub>2</sub>·6H<sub>2</sub>O, Dinâmica<sup>®</sup>, Barueri, Brazil, 98–102%) was prepared. Kinetic studies were accomplished with 0.01 g of HAp into 10 mL of cobalt stock solution. Flame atomic absorption spectroscopy (FAAS) was used to determine the residual unadsorbed Co<sup>2+</sup> concentration at various times (5, 10, 15, 30, 60, 120, 240, 360, 960, 1440, 2880, and 4320 min) employing a PinAAcle 900T (Perkin Elmer<sup>®</sup>, Waltham, United States of America) spectrometer. FAAS instrumental parameters were Co wavelength of 240.73 nm, 0.2 nm slit width, and flame under oxidant flow composed of air (10 L min<sup>-1</sup>) and acetylene (2.5 L min<sup>-1</sup>). Isotherm studies were performed with 0.005 g of HAp in 5 mL of different cobalt-diluted solutions (10, 25, 50, 100, 200, 500, and 1000 mg L<sup>-1</sup>) in distilled water. All tests were repeated three times.

Concerning Co<sup>2+</sup> release, Co-adsorbed HAp (1 mg mL<sup>-1</sup>) was placed into a fertilizer-like “benchmark” 2% w/w citric acid solution and maintained at 40 °C. Co<sup>2+</sup> concentration was monitored by FAAS after 7, 15, 30, 60, 120, 240, 480, 720, 1440, 2880, 5760, and 7200 min. Additionally, phosphorous release from hydroxyapatite was also investigated by UV-Vis spectroscopy through the molybdenum blue-phosphate quantitative method [81–84].

#### 2.5. Cytotoxicity Analysis

Watergrass seeds (20 ± 2 units) were placed in four falcon tubes with 14 mL of distilled water. Three of them also received 28 mg of each HAp sample (F–HAp, HAp\_600 °C, and HAp\_900 °C after cobalt adsorption experiments). All watergrass seeds were maintained immersed for 1 h. After this time, 12 mL of solution were withdrawn carefully, and the adsorbents were separated. Next, four Petri dishes were lined with equally sized filter papers. The watergrass seeds were then placed in these Petri dishes, along with 2 mL of the remaining solution. For three days, the watergrass seeds were kept at room temperature, with natural luminosity in order to grow, and adding water when the paper filter was dry. Watergrass seeds without HAp were called blank (water only). After three days, the roots in contact with each sample were observed by optical microscopy analysis, and the germinated seeds were counted.

### 3. Results and Discussion

#### 3.1. Material Characterization

Diffraction patterns of the hydroxyapatite-based adsorbents are shown in Figure 1a. The International Centre for Diffraction Data (ICDD) card that most adequately matched the experimental peaks for all diffraction patterns was PDF number n. 9-432 [85–88]. This card corresponds to the ISO internationally accepted standard for pure hydroxyl apatite (calcium phosphate hydroxide): Ca<sub>5</sub>(PO<sub>4</sub>)<sub>3</sub>(OH), hexagonal system, and space group P6<sub>3</sub>/m (n. 176). A 95% confidence threshold was initially used. All the indexed peaks for the heat-treated samples (39 peaks for HAp\_600 °C and 48 for HAp\_900 °C) are presented in Figure 1a top panel. Conversely, the pristine F–HAp adsorbent showed no statistically significant matches. Nevertheless, 14 peaks could be assigned to hydroxyapatite despite peak broadening (Figure 1a bottom panel).

FWHM and peak intensity analyses (Figure 1b) were performed on (211) and (022) crystallographic plane signals for all samples. The gradual increase in peak intensity and the significant decrease in the FWHM indicate that material crystallinity improves as the annealing temperature is increased. Such a behavior is consistent with a crystal structure reorganization, without formation of secondary phases, caused by heat treatment and occurring through complete removal of collagen fibers and release of water and carbonate groups (see further below) from the lattice [89,90]. Unit cell parameters were calculated (unit cell program with 95% reliability) for all samples (see Table 2). *a/b* and *c* lattice

constant differences with respect to reference were almost immaterial, with parameter *c* maximum variation equal to 0.48% and 0.40% for samples HAp\_600 °C and HAp\_900 °C, respectively. Therefore, the HAp\_600 °C and HAp\_900 °C materials were assumed to be composed mainly of pure hexagonal HAp.

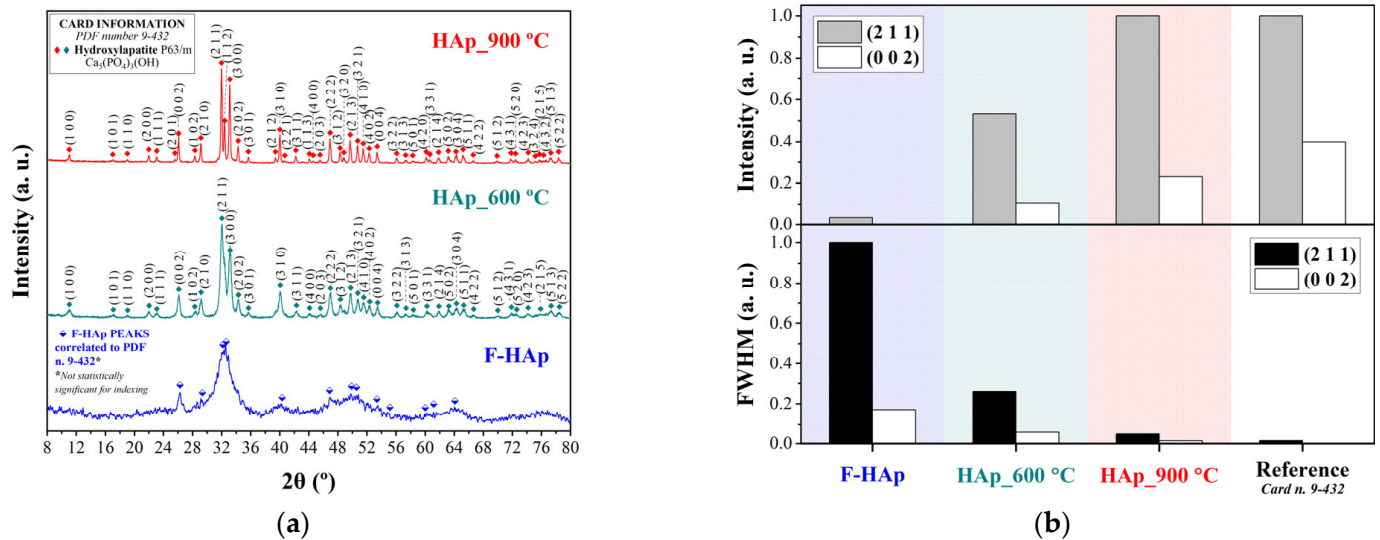


**Figure 1.** X-ray (a) diffractograms of F–HAp, HAp\_600 °C, and HAp\_900 °C, in addition to (b) FWHM and intensity plots for peaks (2 1 1) and (0 0 2).

**Table 2.** Calculated Unit Cell lattice parameters (hexagonal system).

Sample ID\ Unit Cell Parameters	<i>a, b</i> (Å)	<i>c</i> (Å)	<i>c/a</i>	<i>V</i> (Å <sup>3</sup> )
Reference HAp card (PDF n. 9-432)	9.418	6.884	0.7309	528.88
F–Hap *	9.41673 ±0.00093	6.85635 ±0.00065	0.7281	526.5311 ±0.1013
HAp_600 °C	9.38819 ±0.00037	6.85108 ±0.00050	0.7298	522.9424 ±0.0440
HAp_900 °C	9.39021 ±0.00033	6.85898 ±0.00046	0.7304	523.7700 ±0.0395

\* Manually estimated peaks (not statistically significant for a 95% threshold).

Although there was evidence of a hydroxyapatite phase in the untreated sample, F–HAp XRD pattern was affected by poor crystallinity and presence of organic residues bringing about low diffraction intensities and considerable peak broadening. Thus, the purity of F–HAp was estimated to be relatively low due to presence of minority phases. In fact, carbonated hydroxyapatite and collagen are usually associated to biological hydroxyapatites [91]. These things considered, the increase in the *c/a* ratio compared to pristine HAp, approaching the reference HAp for treated samples is typical of B-type carbonated hydroxyapatite, in which carbonate groups replace part of phosphate groups. On the other hand, when carbonate enters the hydroxyl sites, the *c/a* ratio decreases, and an A-Type carbonated hydroxyapatite is formed [92–94]. Thus, *c/a* ratio suggests that a small amount of B-type carbonated hydroxyapatite may also remain in the 900 °C-treated (i.e., more crystalline) sample. Needless to say, HAp\_900 °C presented greater evidence of a pure stoichiometric hydroxyapatite phase belonging to the hexagonal system

and space group P63/m (n.176). For this reason, the three-dimensional structure of the unit cell was constructed in VESTA based on the reference data and on the lattice parameters calculated previously. Renderings of the HAp\_900 °C structure are shown in Figure 2a,b in a ball-and-stick and polyhedral models, respectively.

Figure 3 reports FT–IR spectra of the three adsorbing materials, and the functional groups (i.e., bands) were assigned to each sample as shown in Table 3.

Table 3. FT–IR Spectroscopy for HAp-based materials.

Wavenumber (cm <sup>-1</sup> )	Assignment *	Functional Group **	References
3580	A <sup>a b c</sup>	O-H $\nu_s$ structurally bond, a weak band (HAp)	[92,95]
3300	B <sup>a</sup>	O-H $\nu$ broadband (water)	[95,96]
3000	C <sup>a</sup>		
2916	D <sup>a</sup>	C-H $\nu$ (fats, organic matter)	[95–97]
2836	E <sup>a</sup>		
1640	F <sup>a</sup>	O-H $\delta$ (water) C=O (amide I and collagen)	[95,96] [97–99]
1560	G <sup>a</sup>	Amides I and II	[97–99]
1457	H <sup>a b c</sup>		
1410	I <sup>a b c</sup>	CO <sub>3</sub> <sup>2-</sup> $\nu_{3as}$ (B-type originated)	[96,99]
1302	J <sup>a</sup>		
1216	K <sup>a</sup>	Amides II and III	[97,100]
1088	L <sup>a b c</sup>	CO <sub>3</sub> <sup>2-</sup> $\nu_{1s}$ and PO <sub>4</sub> <sup>3-</sup> $\nu_3$ (PO stretching)	[99,101,102]
1020	M <sup>a b c</sup>	PO <sub>4</sub> <sup>3-</sup> $\nu_3$ (PO stretching)	[89,92,101]
960	N <sup>b c</sup>	PO <sub>4</sub> <sup>3-</sup> $\nu_1$ (PO stretching)	[89,92,101]
872	O <sup>a b c</sup>	CO <sub>3</sub> <sup>2-</sup> $\nu_{2as}$ (B-type originated)	[89,92,96,101]
673	P <sup>a</sup>	C-H $\rho$ (impurities)	[95,103]
631	Q <sup>b c</sup>	O-H $\nu_L$ vibration (HAp), shouldered to PO <sub>4</sub> <sup>3-</sup> $\nu_4$	[101,104]
597	R <sup>a b c</sup>		
560	S <sup>a b c</sup>	PO <sub>4</sub> <sup>3-</sup> $\nu_4$	[101,105,106]
471	T <sup>a b c</sup>	PO <sub>4</sub> <sup>3-</sup> $\nu_2$	[101,107]

\* a = F–HAp, b = HAp\_600 °C and c = HAp\_900 °C; \*\*  $\nu$  (stretch),  $\delta$  (bend), and  $\rho$  (rock) vibrations.

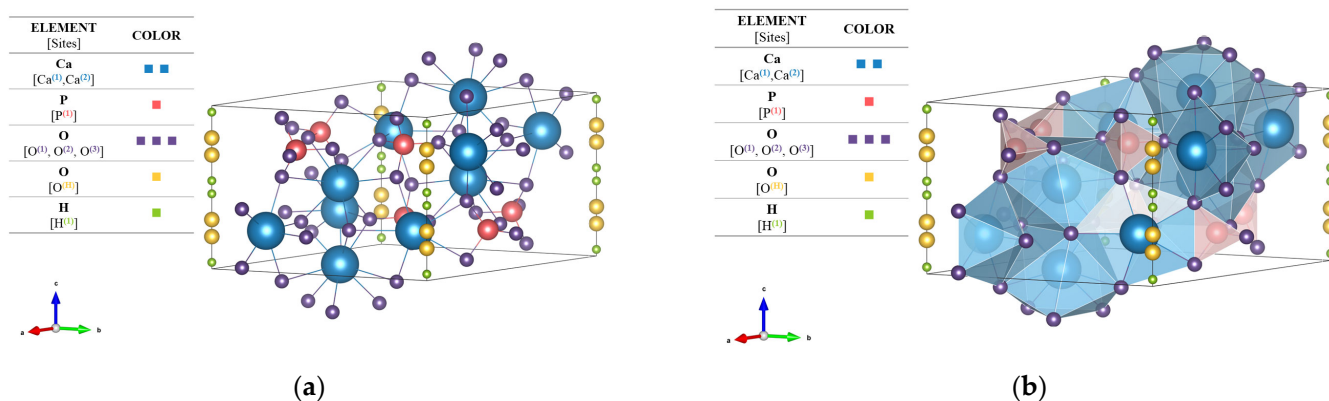
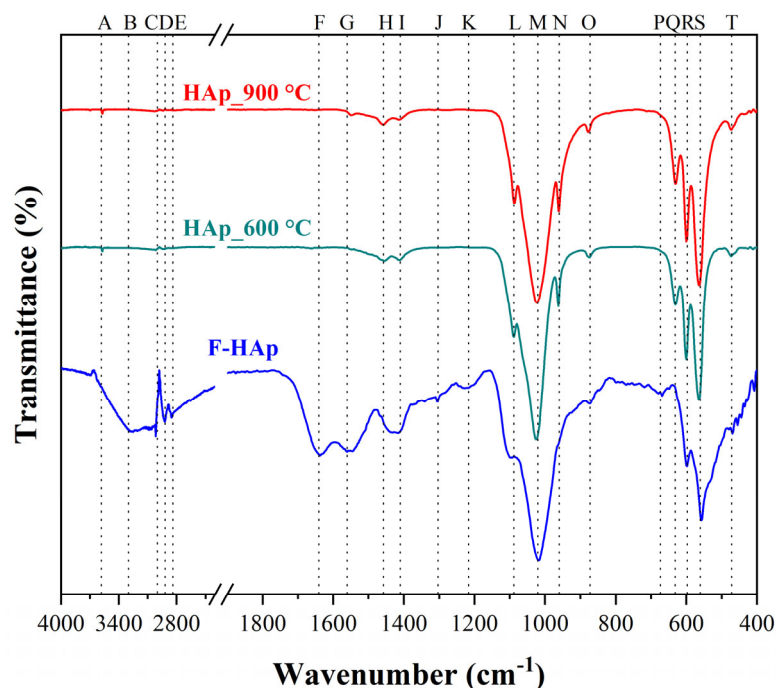


Figure 2. Rendered structural (a) ball-and-stick and (b) polyhedral images of HAp\_900 °C (standard orientation of crystal shape).

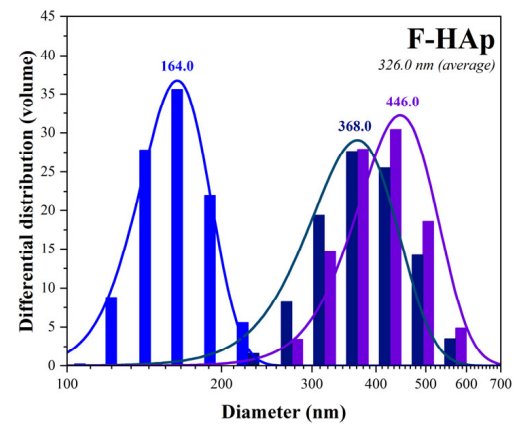
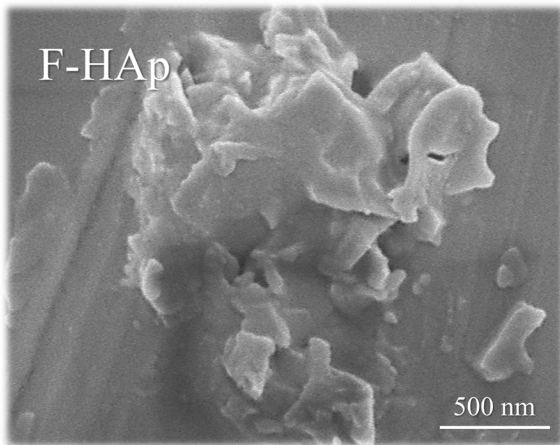


**Figure 3.** FT–IR Spectra for all HAp-based materials.

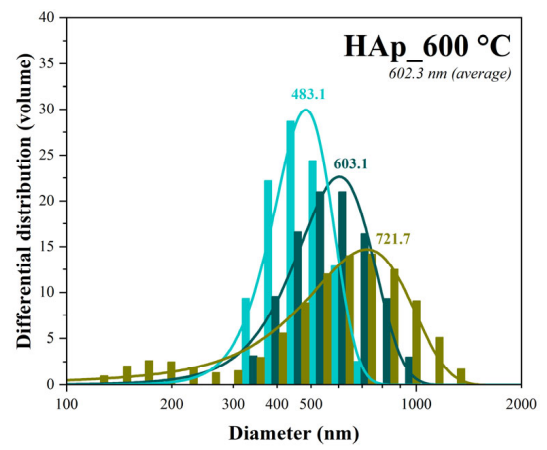
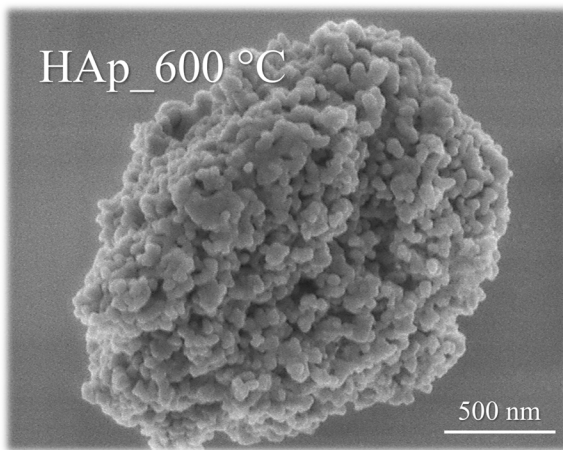
It is worth noticing that the F–HAp adsorbent presents a wide peak broadening between  $1350$  and  $1570\text{ cm}^{-1}$  corresponding to carbonated hydroxyapatite [101], thus confirming the XRD results. Moreover, presence of B-type carbonated hydroxyapatite can also be verified by the  $1457$ ,  $1410$ , and  $872\text{ cm}^{-1}$  bands found in the F–HAp sample. These bands are remarkably close to the  $1455$ ,  $1413$ , and  $874\text{ cm}^{-1}$  absorption peaks related to the  $\nu_{as}$  B-type vibrations originating from the carbonate group [108]. In addition, the usual bands at  $880$  and  $1540\text{ cm}^{-1}$  of A-type carbonated hydroxyapatite were not detected [109]. For all spectra, a low-intensity band associated to the stretching vibration of the structural hydroxyapatite O–H group [A] was also revealed. Therefore, carbonate groups most likely substituted the phosphate group sites (B-type) instead of hydroxyl groups (A-type) [92]. Furthermore, the spectra indicate that the heat treatment promoted the elimination of groups associated with fats and organic impurities [C, D, E, P bands], proteins and collagen [F, G, J, K bands], which were all detected only in the untreated material (F–HAp). Furthermore, the broad band in the region from  $1350$  to  $1570\text{ cm}^{-1}$  disappeared almost completely upon thermal treatment, while additional bands typical of HAp vibrations appeared. In this regard, the characteristic hydroxyapatite structure bands belonging to the phosphate group (e.g., asymmetric stretching  $\nu_3$  [L, M, N] and symmetric stretching  $\nu_4$  [Q, R, S] vibrations) were detected.

DLS (volume basis analysis) and FEG–SEM imaging were used to estimate the adsorbent particle diameter, see Figure 4. The average particle sizes were found to be  $326.0\text{ nm}$ ,  $602.3\text{ nm}$ , and  $620.2\text{ nm}$ , for F–HAp, HAp<sub>600 °C</sub>, and HAp<sub>900 °C</sub>, respectively. Particle agglomeration stemming from heat treatment was also confirmed by SEM micrographs as shown in Figure 4c. In addition, higher annealing temperatures also enhanced particle homogeneity. F–HAp mean diameter distribution turned out to be the widest, from  $164.0$  to  $446.0\text{ nm}$  ( $282.0\text{ nm}$  variation). The range decreased for HAp<sub>600 °C</sub>, from  $483.1$  to  $721.7$  ( $238.6\text{ nm}$  variation), and was the lowest for HAp<sub>900 °C</sub>, from  $666.6$  to  $561.7\text{ nm}$  ( $104.9\text{ nm}$  variation). Such a behavior was related to the increased crystallinity of the samples and to the elimination of organic residues improving particle size uniformity. Thus, the heterogeneity of the particles decreased, and particle agglomeration was favored as the annealing temperature was raised (Figure 4b,c). Nevertheless, all materials are in the sub-micrometric/micrometric range ( $160$  to  $700\text{ nm}$ ) with maximum particle size distributions not exceeding  $1500\text{ nm}$ .

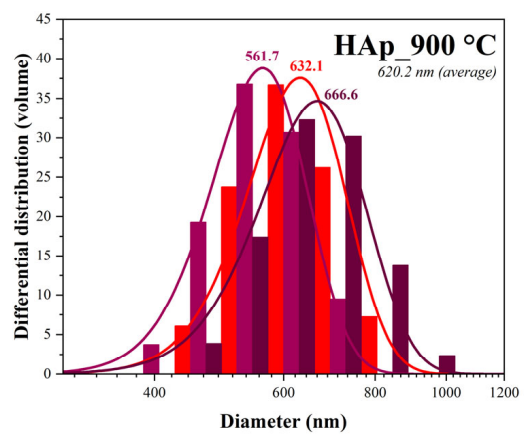
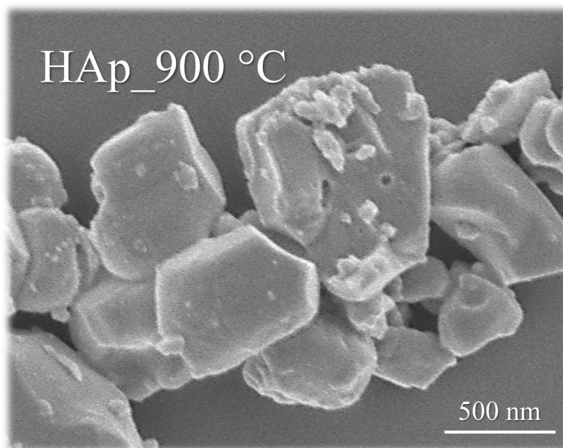




(a)



(b)



(c)

**Figure 4.** FEG–SEM micrographs and DLS measurements for (a) F–HAp, (b) HAp<sub>600 °C</sub>, and (c) HAp<sub>900 °C</sub>.



Zeta potential analysis was performed to verify the stability of the particles in water. Results are shown in Table 4.

**Table 4.** Zeta potential measurements.

Sample ID	pH	Zeta Potential (ZP)
F-HAp	6.2	−20.3 mV
HAp_600 °C	6.7	−4.6 mV
HAp_900 °C	6.2	−0.7 mV

Zeta potential data corroborated the findings regarding particle heterogeneity. Hence, deviations from measured values narrowed as the heat treatment temperature increased. None of the samples reached solution stability condition (approximately  $\pm 30$  mV [110]). The average surface charge values were slightly negative, and all samples' isoelectric points were close to neutral pH, indicating a tendency of the particles to agglomerate in aqueous media. In accordance with the literature, HAp particles close to the isoelectric point in a neutral aqueous medium tend to form clusters [111]. Nonetheless, F-HAp unusually high ( $\approx 20$  mV) zeta potential value coupled to small (i.e., less agglomerated) particle size (compared to other samples) is supposed to originate from ionization of amino acid groups and steric stabilization due to collagen residues.

The thermal stability of the hydroxyapatite-based materials and the elimination temperature of organic residues were further investigated by thermogravimetric analysis (TG/dTG curves) presented in Figure 5.

Weight loss percentages corresponding to each thermal event (loss of adsorbed and lattice water, loss of organic matter, and losses attributed to inorganic material) are summarized in Table 5, along with total weight loss for the entire temperature range (25–900 °C).

**Table 5.** Weight loss of each reported thermal event (thermogravimetric analysis).

Sample ID	Weight Loss (%)			
	25–200 °C (Water)	200–550 °C (Organic)	550–900 °C (Inorganic)	25–900 °C (Total Weight Loss)
F-HAp	11.7	33.8	1.24	46.7
HAp_600 °C	1.42	0.78	1.49	3.69
HAp_900 °C	0.23	0.46	0.73	1.41

The highest weight loss (46.7%) was reported for the thermally unprocessed sample. This material is comprised of water (physically and chemically adsorbed), fat, proteins, collagen, and other organic and inorganic compounds. As observed by FT-IR, most of these compounds are not detected after heat treatments above 600 °C. Consequently, weight loss of the heat treated (HAp\_600 °C and HAp\_900 °C) samples is almost negligible [112]. As expected, HAp\_900 °C showed the smallest weight loss (1.41%). Water loss in biogenic hydroxyapatites (usually B-type carbonated hydroxyapatites) may take place over a wide range of temperatures. Because of point defects (principally vacancies) within the crystal, more than one water molecule and different ion can enter the hydroxyapatite lattice in order for the structure to be stabilized [113,114]. For instance, charge imbalance stemming from phosphate replacement with carbonate may allow different hydrated anions to be incorporated into hydroxyapatite [115,116]. Thus, water elimination required no less than 200 °C to be accomplished. Not surprisingly, F-HAp showed the highest water weight loss. The second thermal event was linked to the loss of organic matter [112]. In particular,

there was the elimination of fats and proteins (up to 300 °C), collagen denaturation (from 250 to 350 °C), and collagen degradation/evaporation (from 350 to 550 °C) [90,117–120]. These events were observed for F–HAp and are clearly visible in the dTG curve (Figure 5b). On the other hand, HAp\_600 °C and HAp\_900 °C weight loss is considered almost immaterial (0.8% and 0.5%, respectively) and might be associated to post-synthesis adsorbed organic impurities.

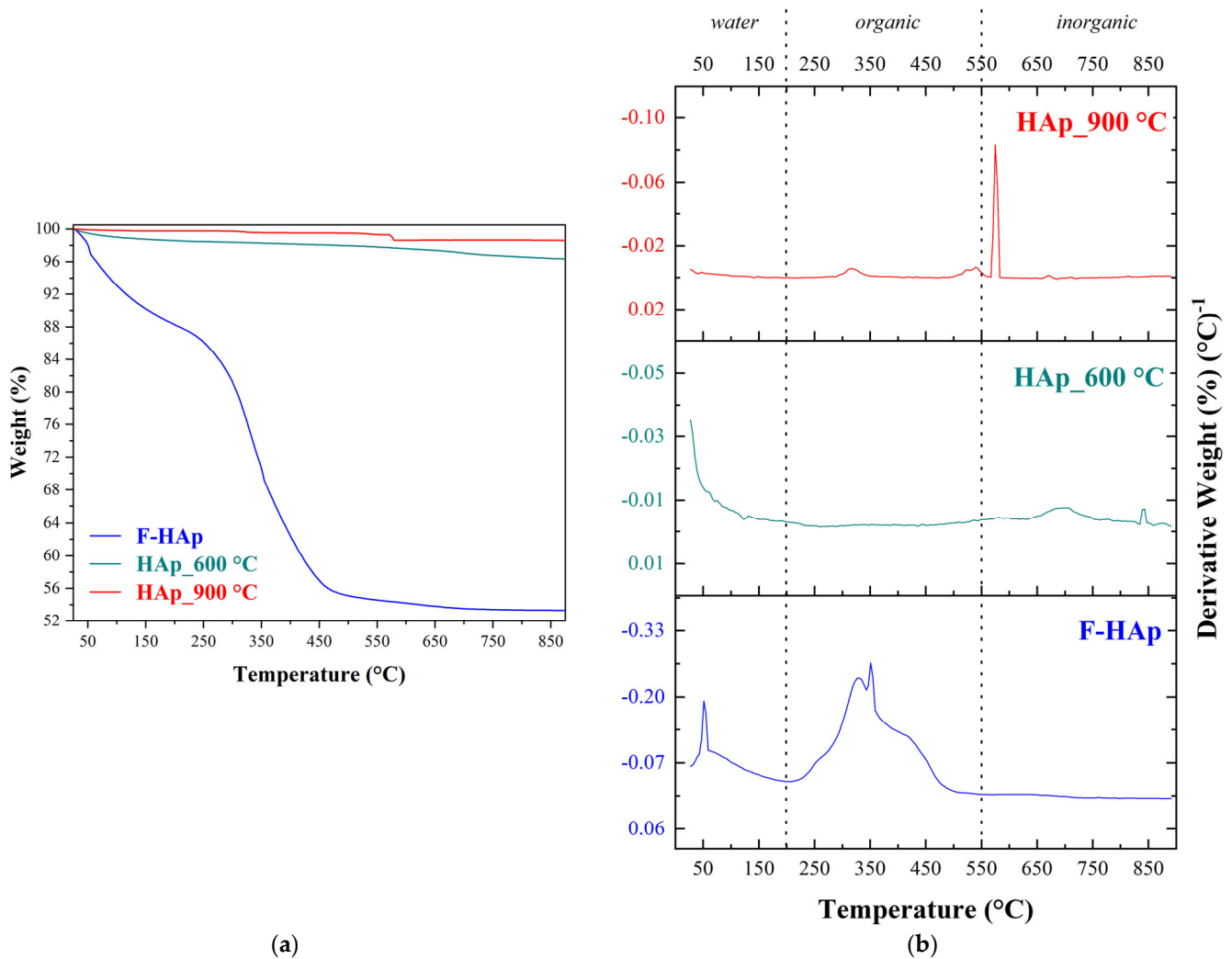
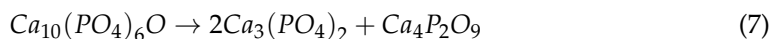
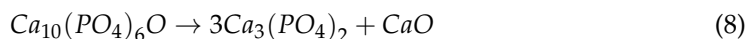


**Figure 5.** (a) Thermogravimetric Analysis (TG) of F–HAp, HAp\_ 600 °C and HAp\_900 °C and their (b) first derivative curves (dTG).

The last event is connected to the hydroxyapatite partial decomposition [121,122]. Thus, two hydroxyl groups join expelling a water molecule and a peroxide ion ( $\text{O}_2^{2-}$ ) in the process. The usual temperature for this process is around 850 °C [122,123], but Ca/P variations in the structure (even locally) can accelerate water elimination and lower the decomposition temperature [124–126]. Consequently, a partially dehydroxylated hydroxyapatite, known as OAp,  $\text{Ca}_{10}(\text{PO}_4)_6\text{O}$  [119,127] is formed. OAp is relatively stable between 800 and 1050 °C [128,129]. OAp subsequent decomposition proceeds through two different patterns. The first, described by Equation (7) [119], accounts for the formation of a TTCP (tetra calcium phosphate)/ $\beta$ -TCP (tricalcium phosphate) mixture [119]:



$\beta$ -TCP do not decompose below 1200 °C. The second degradation pathway (Equation (8) [119]) produces a mixture of TCP (tricalcium phosphate) and CaO (calcium oxide).



Both transformations involve no mass alteration. Therefore, OAp generation (i.e., hydroxyapatite dihydroxylation) is solely responsible for weight loss above 600 °C.

### 3.2. Adsorption Experiments: Kinetic Models

Experimental results regarding kinetic (i.e., time dependence) tests for ATZ and  $\text{Co}^{2+}$  adsorption on HAp-based materials are presented in Figure 6.

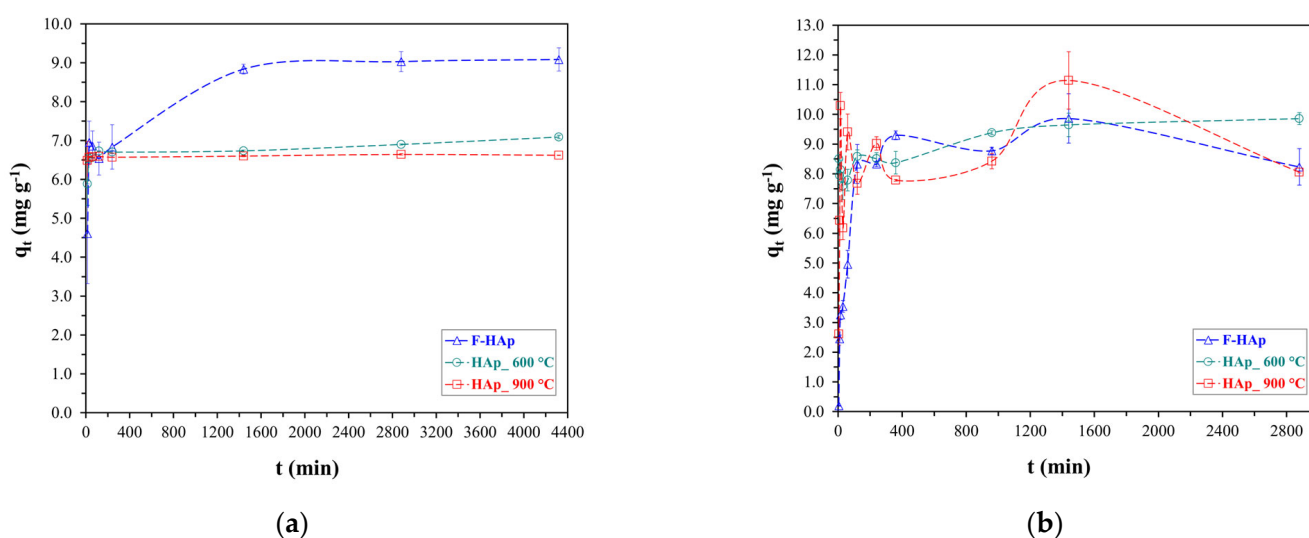


**Figure 6.** Variation of adsorption capacity versus time for (a) atrazine and (b) cobalt adsorption.

Due to the different nature of the two water contaminants, equilibration time turned out to be quite different. Considering the full three-set of samples, equilibrium was reached after approximately 1600 min (26.7 h) for atrazine, while it took around 400 min (3.7 h) for cobalt adsorption to stabilize (by taking into account experimental errors). F-HAp (Figure 6a) showed high atrazine adsorption capacity ( $9.0 \text{ mg g}^{-1}$ ) compared to HAp\_600 °C and HAp\_900 °C (about  $6.5 \text{ mg g}^{-1}$ ), although more time was needed to reach equilibrium (1600 min versus  $\approx 400$  min). The enhanced F-HAp atrazine adsorption behavior can be ascribed to the organic impurity residues (mostly collagen) that remained on the surface of the raw material. In fact, collagen can reasonably provide plenty of C=O moieties (stemming from amino acids arranged in chains) capable of establishing H-bonds with atrazine N-H groups. Water can also compete with collagen to form hydrogen bond with atrazine and can intercalate between amino acid chains by dint of the same kind of mechanism. Furthermore, collagen residues are expected to interact by means of weak Van der Waals forces with the atrazine heteroaromatic ring. However, F-HAp superior performances were lost for higher concentration of atrazine, as discussed by the adsorption isotherm study further below.

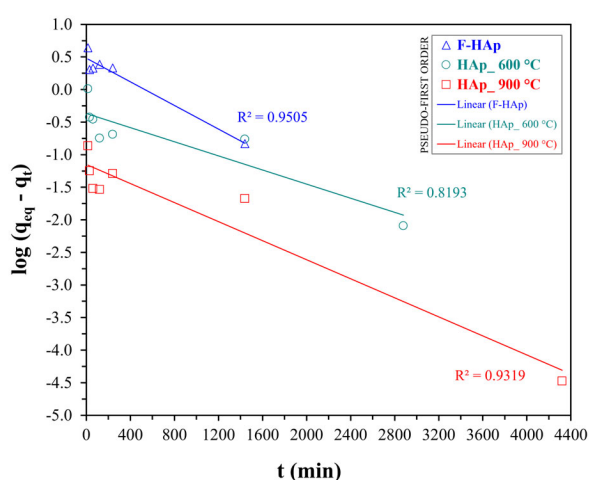
On the other hand, similar adsorption capacities among the different hydroxyapatite-based materials were found for  $\text{Co}^{2+}$ . Cobalt ion removal from aqueous solutions by hydroxyapatite has already been reported to take place mainly by ion exchange with calcium [130–134] and therefore,  $\text{Co}^{2+}$  adsorption on all HAp samples is supposed to be facilitated. Nonetheless, physisorption always overlaps to ion exchange causing adsorption

to occur through different pathways and resulting in a less stable kinetic profile (more significant deviations). Thereby, parameters related to the adsorbent surface availability need to be factored in despite close adsorption capacities (see Section 3.2).

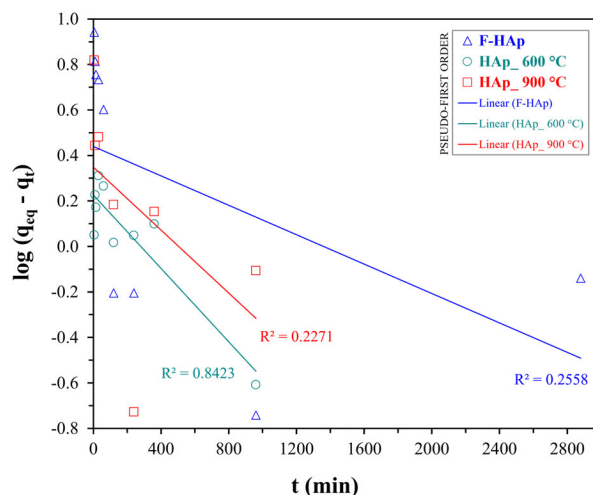
Kinetic data for both pollutants were fitted with pseudo-first (see Figure 7) and pseudo-second order (see Figure 8) models. The values of the pseudo-first order ( $k_{1st}$ ) and pseudo-second order ( $k_{2nd}$ ) rate constants, the initial adsorption rate ( $h_0$ ) for the pseudo-second order kinetics, the calculated values of adsorption capacity at equilibrium ( $q_{eq}$ ), and the quality of the fit ( $R^2$ ) are provided in Table 6.

**Table 6.** Calculated pseudo-first order and pseudo-second order kinetics parameter values for all adsorbents (F-HAp, HAp\_600 °C, and HAp\_900 °C) and pollutants (atrazine and cobalt).

Kinetics \ Sample ID	Atrazine Adsorption			Cobalt Adsorption			
	F-HAp	HAp_600 °C	HAp_900 °C	F-HAp	HAp_600 °C	HAp_900 °C	
Pseudo-first order	$k_{1st}$ (min <sup>-1</sup> )	0.002073	0.001152	0.001612	0.0006909	0.001842	0.001612
	$q_{eq}$ (mg g <sup>-1</sup> )	3.039	0.4300	0.07047	2.750	1.682	2.233
	$R^2$	0.9505	0.8193	0.9319	0.2558	0.8423	0.2271
Pseudo-second order	$k_{2nd}$ (g min <sup>-1</sup> mg <sup>-1</sup> )	0.003030	0.009343	0.1657	0.004131	0.004824	0.009407
	$q_{eq}$ (mg g <sup>-1</sup> )	9.141	7.042	6.627	8.658	9.852	8.569
	$h_0$ (mg min <sup>-1</sup> )	0.2532	0.4633	7.2771	0.3097	0.4682	0.6907
	$R^2$	0.9998	0.9996	1.000	0.9881	0.9994	0.9830
EXPERIMENTAL ADSORPTION CAPACITY $q_{obs}$ (mg g <sup>-1</sup> )		8.98	6.91	6.62	8.95	9.63	9.21



(a)



(b)

**Figure 7.** Linear fitting plots of pseudo-first order kinetic model for (a) atrazine and (b) cobalt adsorption.

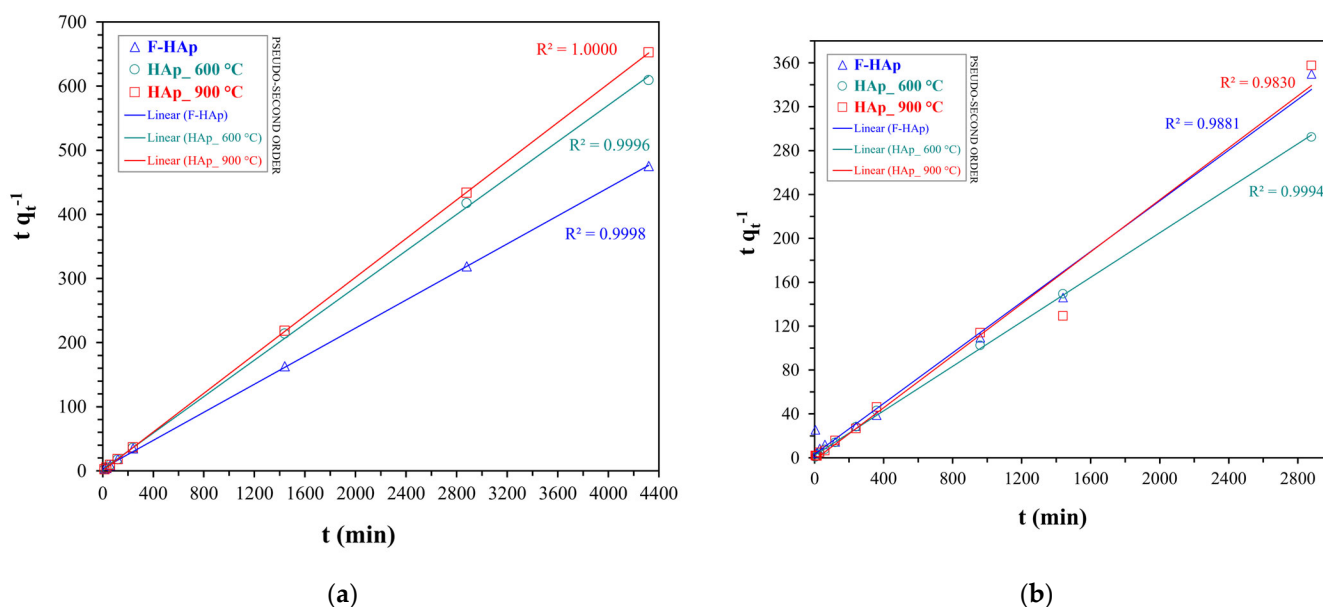


**Figure 8.** Linear fitting plots of pseudo-second order kinetic model for (a) atrazine and (b) cobalt adsorption.

The pseudo-second order model was discovered to be the best kinetic fit for both cobalt and atrazine adsorption accounting for the behavior of all HAp, as proved by the higher  $R^2$  and by the good agreement between experimental and calculated  $q_{eq}$  values. Conversely, pseudo-first order fit underestimated the equilibrium adsorption capacity for all the adsorbents, notwithstanding an  $R^2$  value close to one.

In addition, the pseudo-second order model successfully described the slow atrazine adsorption kinetics (lower  $h_0$  and  $k_{2nd}$ ) showed by F–HAp. In addition, F–HAp kinetic parameters were the lowest also in the case of  $Co^{2+}$  adsorption. Indeed, the high steric hindrance brought about by the collagen residues may retard cobalt approximation to the inner part of the adsorbent hampering ion exchange and reflecting longer equilibration times. However, adsorption on F–HAp may still benefit from  $Co^{2+}$  coordination by amino acid groups and residual (physisorbed and structural) water. In fact, F–HAp  $q_{eq}$  is in line with the corresponding values of the thermally treated adsorbents. On the contrary, HAp\_900 °C presented the highest adsorption rate coupled to the lowest  $q_{eq}$  for both atrazine and  $Co^{2+}$ . Not surprisingly, particle coalescence deriving from thermal annealing can limit atrazine and cobalt adsorption to the external surface of the material. Consequently, adsorption equilibrium can be achieved fairly quickly at expenses of adsorption capacity.

Adsorption isotherms were additionally studied in order to further investigate adsorption capacities of the HAp-based materials, their dependence on the pollutant initial concentration as well as the adsorption favorability and the removal capability for each of the two contaminants.

### 3.3. Adsorption Experiments: Isotherm Models

Equilibrium adsorption capacity versus initial pollutant concentration graphs are reported in Figure 9 for both atrazine (Figure 9a) and  $Co^{2+}$  (Figure 9b).

Experimental curves for the two different contaminants were found to be substantially different underlying two distinct adsorption mechanisms. Regarding McCabe’s plots [135] for the experimental isotherms, atrazine presented a practically linear profile up to an equilibrium concentration of approximately  $60 \text{ mg L}^{-1}$ . Considering this equilibrium concentration, the adsorption capacity by graphical extrapolation of the experimental data was approximately  $10 \text{ mg g}^{-1}$ ,  $11 \text{ mg g}^{-1}$ , and  $21 \text{ mg g}^{-1}$  for F–HAp, HAp\_600 °C, and



HAp\_900 °C, respectively. It can be speculated that as ATZ concentration increased, the number of collagen residues on the F–HAp material available for interaction (by Van der Waals forces or H-bond) with the herbicide decreased. Seeing as atrazine is a relatively large molecule, penetration of the herbicide in the F–HAp internal part is to be presumably hindered by collagen residues when the contaminant concentration is increased (i.e., molecular crowding). Furthermore, the formation of hydrogen bonds between atrazine N-H groups (disfavoring interaction with the adsorbent) cannot be excluded. Since atrazine is usually present as traces in treated wastewater, F–HAp can still be considered for the removal of this agrochemical (see Figure 6). On the other hand, heat-treated samples were able to adsorb higher amounts of atrazine. Differences between HAp\_600 °C and HAp\_900 °C can be attributed to the partial elimination of OH groups from the hydroxyapatite due to thermal annealing (see Section 3.1). Therefore, higher heat treatment temperatures should raise the degree of dehydroxylation of the HAp surface facilitating the interaction with atrazine (i.e., a hydrophobic molecule). Because of the relatively low level of dehydroxylation of both heat-treated samples, the differences between HAp\_600 °C and HAp\_900 °C in adsorption capacity tend to be reduced as the atrazine initial concentration increases and thus, dehydroxylated sites are progressively occupied.

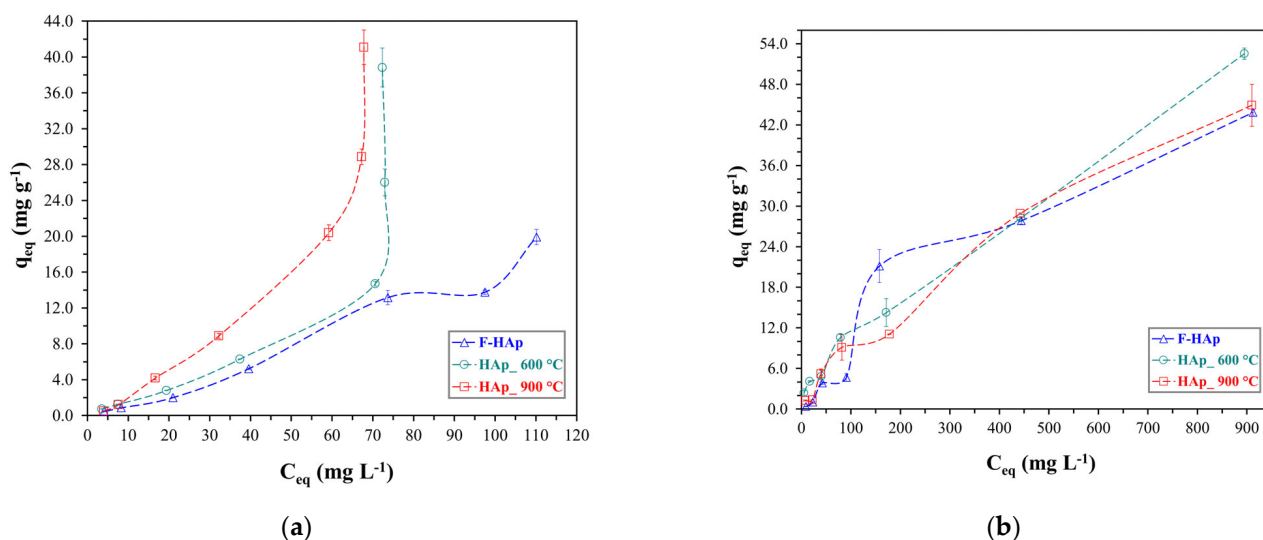


**Figure 9.** Experimental isotherms (not fitted) for (a) atrazine and (b) cobalt adsorption.

Concerning cobalt adsorption, the curves were favorable throughout the entire range of the explored  $\text{Co}^{2+}$  initial concentrations, even though presenting approximately linear regions. Graphical extrapolation on the last common point (with a  $\text{Co}^{2+}$  equilibrium concentration of  $880 \text{ mg L}^{-1}$ ) revealed adsorptive capacity values of about  $52 \text{ mg g}^{-1}$  for HAp\_600 °C,  $44 \text{ mg g}^{-1}$  for HAp\_900 °C, and  $42 \text{ mg g}^{-1}$  for F–HAp. The largest  $q_{eq}$  values observed, especially at high  $C_{eq}$ , for HAp\_600 °C can be justified by allowing for the different level of  $\text{Co}^{2+}$  penetration into the internal part of the adsorbing material. In fact, particle coalescence almost precludes cobalt adsorption in the inner portion of the HAp\_900 °C sample. Similarly to ATZ, collagen may obstruct  $\text{Co}^{2+}$  access to the F–HAp internal surface. Conversely, HAp\_600 °C inner pores are mostly available for cobalt adsorption. To further understand the behavior of each sample, Figure 9 plots were fitted to Langmuir and Freundlich isotherms (linear equations). The Langmuir linear fits for the HAp samples are shown in Figure 10 for both pollutants, whereas Freundlich model linear fits (also for both pollutants) are shown in Figure 11.

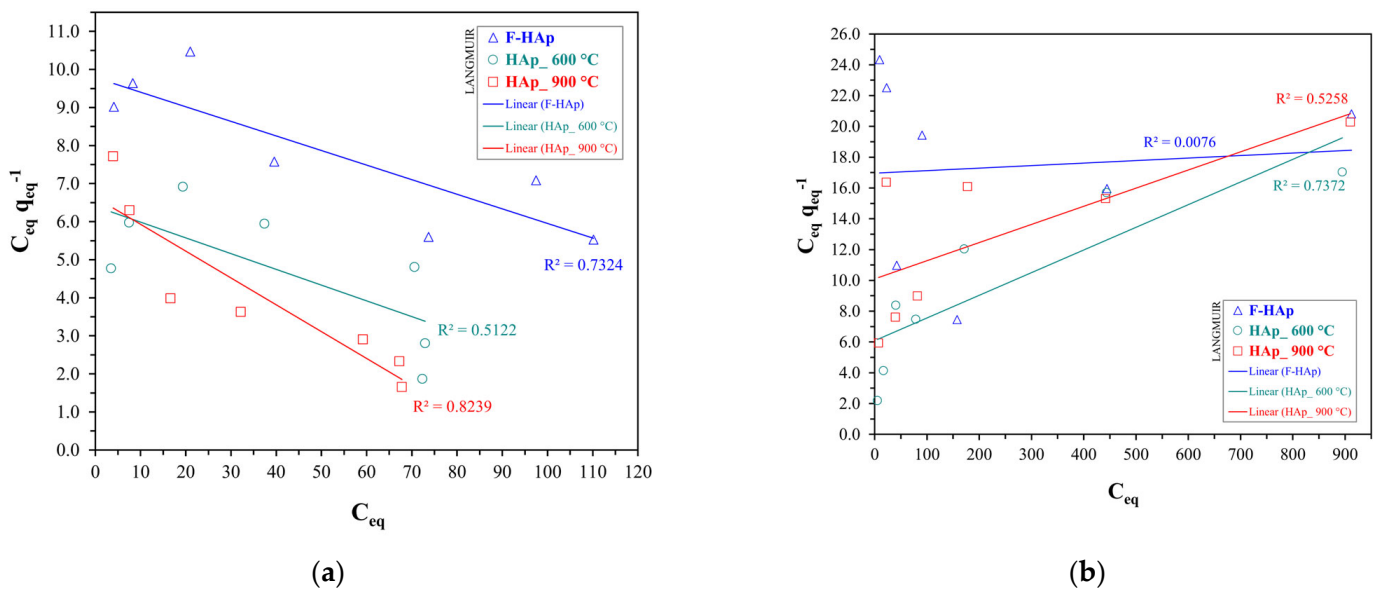


Figure 10. Linear fitting plots of Langmuir isotherm model for (a) atrazine and (b) cobalt adsorption.

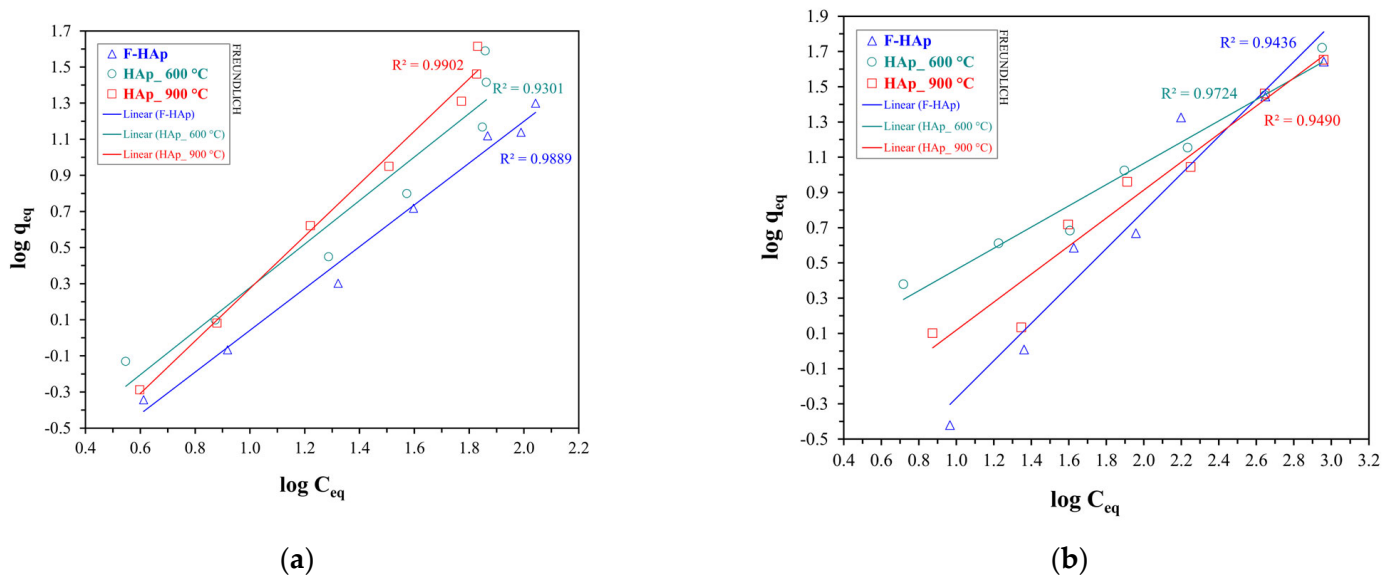


Figure 11. Linear fitting plots of Freundlich isotherm model for (a) atrazine and (b) cobalt adsorption.

Freundlich model was found to fit best the adsorption isotherms for all samples and both pollutants. Langmuir adsorption is predicated on energy equivalent adsorption sites, and on the formation of a monolayer as the only adsorption model [79,136–138]. Needless to say, such a model can be hardly applied to highly heterogeneous bio-derived HAp surfaces. Thus, the Freundlich model, accounting for adsorption site heterogeneity and energy distribution differences [80,136,138], was more adequate to describe adsorption on HAp regardless of the pollutant. Fit salient parameters are reported in Table 7 along with the assigned favorability of the adsorption process (Freundlich). Isotherm favorability was determined according to the literature, where  $0 < 1/n < 1$  is assigned for a favorable (F) adsorption process and  $1/n > 1$  for when the adsorption is unfavorable (U). Furthermore,  $n$  also represents the heterogeneity in the adsorption process. The higher  $n$  is, the higher the difference in energy and capability of active sites for adsorption [80,136,138].

**Table 7.** Calculated Langmuir and Freundlich isotherm model parameters for all adsorbents (F–HAp, HAp\_600 °C, and HAp\_900 °C) and pollutants (atrazine and cobalt).

Kinetics\Sample ID		Atrazine Adsorption			Cobalt Adsorption		
		F–HAp	HAp_600 °C	HAp_900 °C	F–HAp	HAp_600 °C	HAp_900 °C
Langmuir	$K_{Lg}$ (L mg <sup>-1</sup> )	−0.003924	−0.006467	−0.01062	0.00009431	0.002412	0.001168
	$q_{max}$ (mg g <sup>-1</sup> )	−26.04	−24.15	−14.18	625.0	68.03	84.75
	$R_L$	0.9073	0.8649	0.8691	0.9443	0.8590	0.9099
	$R^2$	0.7324	0.5122	0.8239	0.0076	0.7372	0.5258
Freundlich	$K_{Fr}$ (mg g <sup>-1</sup> )	0.07654	0.1182	0.06618	0.04707	0.7244	0.2108
	$n$	0.8637	0.8297	0.6885	0.9430	1.660	1.258
	$1/n$	1.158	1.205	1.453	1.061	0.6024	0.7949
	$R^2$	0.9889	0.9301	0.9902	0.9436	0.9724	0.9490
FREUNDLICH FAVORABILITY		U	U	U	U	F	F

As for atrazine adsorption,  $1/n$  values were all higher than one. This result can be attributed to the competition between atrazine and water for adsorption on HAp sites. Pristine hydroxyapatite showed the largest  $n$ , as expected for an extremely heterogeneous material characterized by collagen and organic polymers anchored on the hydroxyapatite surface. On the other hand,  $Co^{2+}$  adsorption was predominantly favorable. As previously mentioned,  $Co^{2+}$  adsorption on hydroxyapatite has been widely reported to be facilitated by ion exchange [130,131,133,134]. Hence, both HAp\_600 °C and HAp\_900 °C adsorption isotherms could be fitted by using  $1/n$  values between 0 and 1. The higher cobalt affinity for HAp\_600 °C (i.e., lower  $1/n$ ) can be explained in terms of particle size. In fact,  $Co^{2+}$  adsorption (i.e., ion exchange) into the material internal sites is most likely to occur in the HAp\_600 °C sample rather than in HAp\_900 °C. In addition,  $n$  decreased from HAp\_600 °C to HAp\_900 °C, thus confirming particle coalescence and higher particle surface homogeneity stemming from thermal treatment, as described in Section 3.1. Although high-purity biogenic hydroxyapatite synthesized by bacteria has already been reported to have a considerable affinity for cobalt ions [132], F–HAp presented the largest  $1/n$  (slightly greater than 1), besides possessing the lowest values in terms of adsorption capacity. Indeed, collagen and other organic impurities were possibly responsible for creating a physical barrier to adsorption on the material internal sites, hindering the access to the F–HAp inner part, and favoring adsorption on the most external sites. Nevertheless, an almost linear adsorption profile (differing from the atrazine case) was maintained. Therefore,  $Co^{2+}$  small size (compared to ATZ) probably allowed a conspicuous number of ions to be accommodated on the F–HAp collagen residues by taking advantage of cobalt coordination by ionized amino acid groups and water molecules.

For comparisons with the literature, experimental graphs were used, and the confrontations were made by interpolation of these data. Ferri et al. [139] synthesized pure stoichiometric HAp by coprecipitation and applied it to the adsorption of cobalt ions. For the isotherm assay, they obtained experimental results of about 0.28 mmol/g (16 mg Co/g HAp) for an equilibrium concentration of 9.0 mmol/L (530 mg/L). By interpolation at the same concentration, the capacities of the HAp samples of this paper were 31 mg/g

(F-HAp), 33 mg/g (HAp\_600 °C), and 32 mg/g (HAp\_900 °C), which is indicative of higher values of adsorption capacities (almost doubled). This higher value is consistent with the work of Handley-Sidhu et al. [140], in which bio-hydroxyapatite showed higher values of cobalt ion adsorption in all media studied compared to synthetic hydroxyapatite. Other studies also found this same tendency [141,142], justifying studies of biogenic-based hydroxyapatites for multifocal adsorption purposes. In the scientific reports study with bio-hydroxyapatite [140], the best fit for the isotherm for cobalt was also Freundlich, which was the only fit with correlation coefficient values greater than 0.95, which further corroborates the findings of this paper.

### 3.4. Release Assays: Cobalt and Phosphorus

Phosphate and cobalt ion release assays from the Co-loaded HAPs are shown in Figure 12.

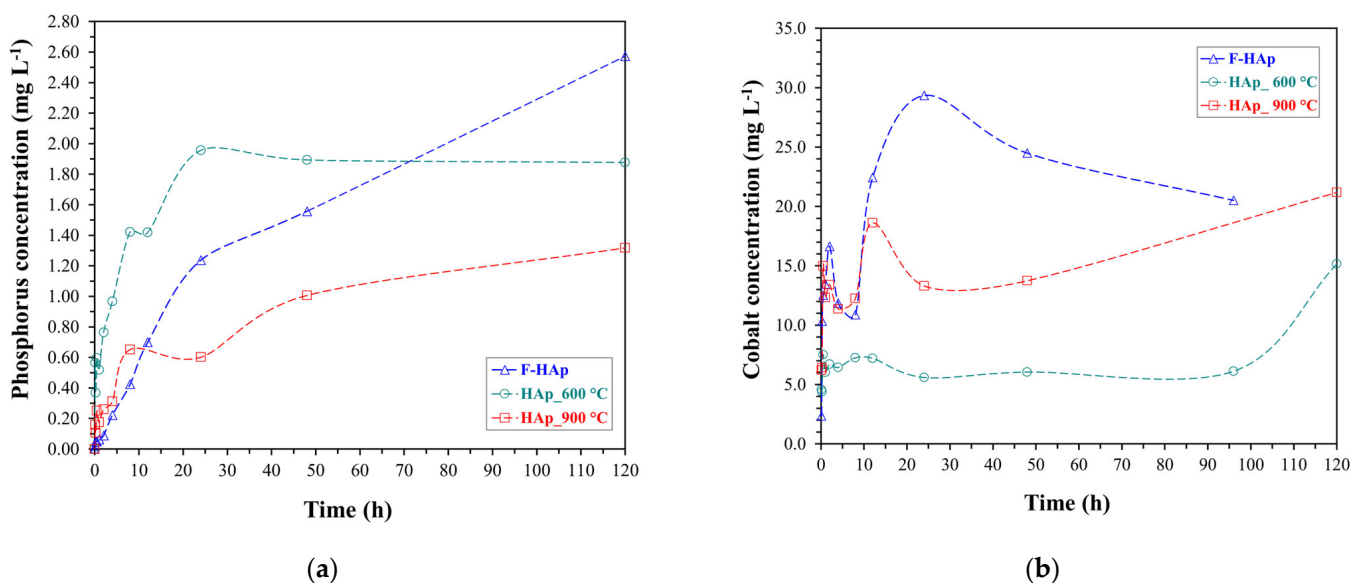


**Figure 12.** (a) Phosphorus and (b) Cobalt release assays by extraction in citric acid medium.

A decent  $\text{PO}_4^{3-}$  amount started being released after 48 h for all sample, topping to  $2.6 \text{ mg L}^{-1}$  for F-HAp. However, HAp\_600 °C released a significant quantity of phosphate (about  $2 \text{ mg L}^{-1}$ ) within the first 48 h. HAp\_900 °C phosphorus release during the early stages of the assay was practically negligible instead. Thus, it can be deduced that reduced particle size and lack of steric hindrance (i.e., no organic residues) were instrumental in enabling  $\text{PO}_4^{3-}$  solubilization through contact with the citric acid solution. In addition, phosphate release is supposed to be aided by the presence of structural defects [143]. Consequently, the formation of a highly crystalline structure brought about by intense heat-treatment might have delayed phosphate liberation from HAp\_900 °C. Concerning F-HAp, surface coverage by organic molecules (including collagen) and competition with carbonate for  $\text{H}^+$  from citric acid may have slowed down  $\text{PO}_4^{3-}$  release [144,145].

Regarding  $\text{Co}^{2+}$ , the ion liberation reflected almost perfectly the cobalt available on the adsorbent surface related to sample affinity for cobalt and therefore, the interaction features discovered with the adsorption tests. F-HAp and HAp\_900 °C showed the highest amount of desorbed  $\text{Co}^{2+}$  ions, with values of 22 to 30  $\text{mg L}^{-1}$  and 10 to 20  $\text{mg L}^{-1}$ , respectively. Not surprisingly, cobalt adsorption on external sites (such as in F-HAp and HAp\_900 °C) resulted into a fast  $\text{Co}^{2+}$  release. In particular, pristine hydroxyapatite was prone to a desorption/re-adsorption behavior being the  $\text{Co}^{2+}$ -F-HAp interaction based on ion coordination by means of outer-collagen residues rather than on ion exchange. On the contrary, the high  $\text{Co}^{2+}$  affinity for HAp\_600 °C, deriving from adsorption in the material inner pores, caused a meaningful cobalt release ( $>6 \text{ mg L}^{-1}$ ) only after nearly 100 h.

Since the volume used for release was 0.01 L and the quantity of HAp involved was 0.01 g, the numerical values presented for the released cobalt concentration, in  $\text{mg L}^{-1}$ , are equivalent to the values of its desorption capacity, in  $\text{mg g}^{-1}$ . Therefore, the maximum cobalt desorption capacities for the entire period were 29  $\text{mg g}^{-1}$  (F-HAp), 15  $\text{mg g}^{-1}$  (HAp\_600 °C), and 21  $\text{mg g}^{-1}$  (HAp\_900 °C).

### 3.5. Cytotoxicity Analysis

The cytotoxic assay aimed to evaluate nutrient release effects on seed germination. Visual outcomes are displayed in Figure 13, whereas a summary of the results is reported in Table 8. Seed exposure to F-HAp and HAp\_600 °C still preserved germination activity. These things considered, both samples improved the germination rate from about 52% (water) to 63% (F-HAp) and 78% (HAp\_600 °C). Such result can be attributed to  $\text{Co}^{2+}$  and even more importantly  $\text{PO}_4^{3-}$  release from the Co-loaded HAp.

**Table 8.** Germination viability for watercress seeds exposed to Co-adsorbed HAp obtained from fishery waste.

Data \ Sample ID	Blank (Water)	F-HAp	HAp_600 °C	HAp_900 °C
Total seeds	21	19	18	19
Germinated seeds	11	12	14	2
Viability percentage (%)	52	63	78	10

However, an opposite tendency was found for HAp\_900 °C, with a toxicity effect leading to a decrease in germination viability from 52% (water) to 10%.

Optical microscopy images of the roots from the cytotoxic assay (Figure 13) demonstrated the influence of the HAp materials after a 4-day germination period. Images showed that roots from the blank (water), F-HAp, and HAp\_600 °C samples were more elongated than the HAp\_900 °C ones, suggesting the consequential low development of seeds that germinated in an unfavorable environment. Indeed, HAp\_900 °C large particle dimensions induced sedimentation of the adsorbent on the seeds impeding proper germination and root growth. Detrimental effects on seed germination and root growth might also be associated to HAp\_900 °C increased crystallinity that keeps hydroxyapatite from dissolving in neutral solutions. Although germination behavior parallels the nutrient release in a (Figure 12) citric acid extractive medium (as in most common fertilizer formulations), phosphate liberation tends to decrease in pure water. For instance, Sciena et al. [143] availability of phosphate ions from pure (i.e., stoichiometric) HAp is great in mildly acidic conditions compared to neutral pH.



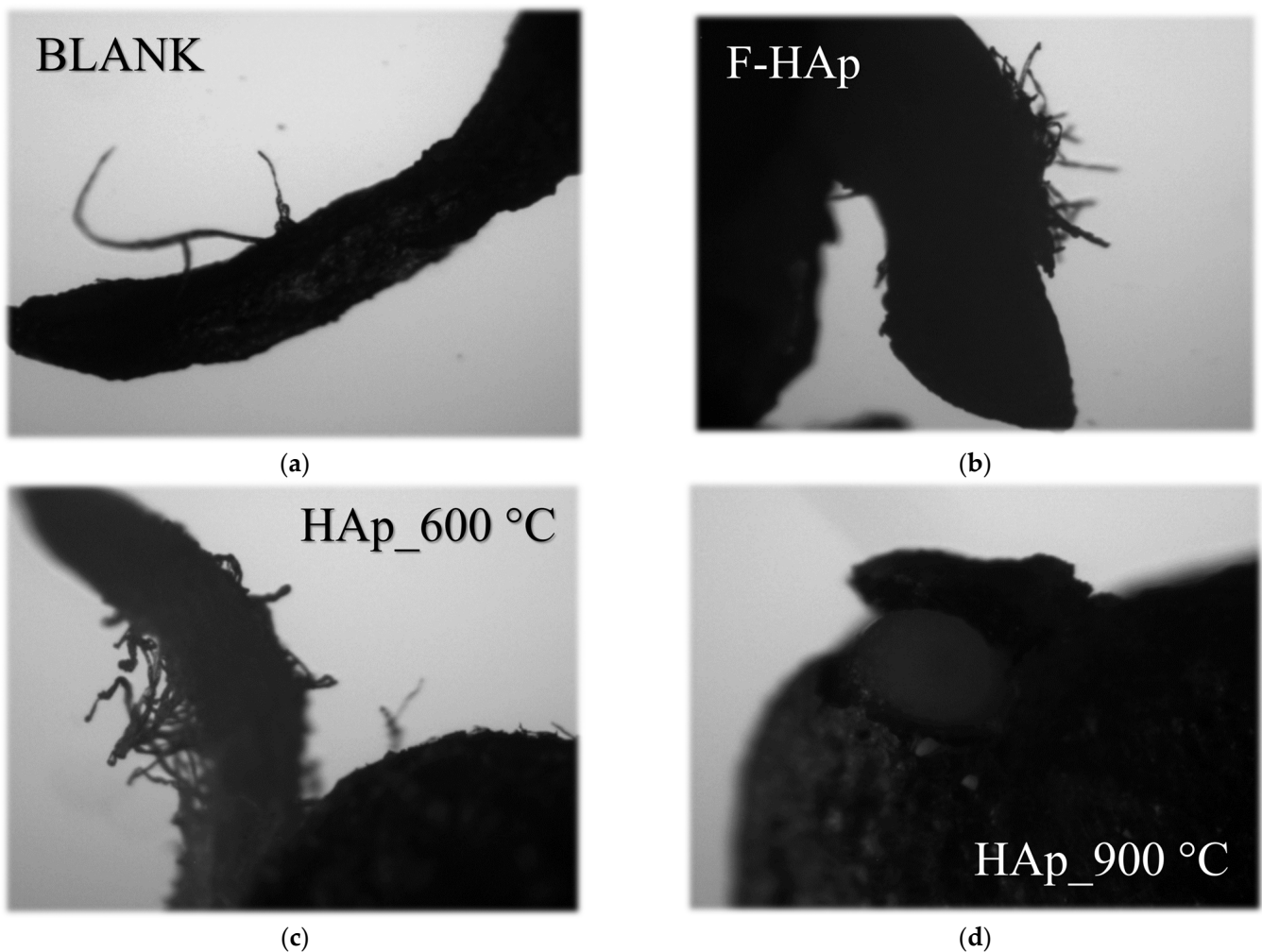


**Figure 13.** Optical microscopy images of watercress roots after a 4-day germination period of seeds exposed to (a) water (blank) and to the Co-adsorbed HAp samples (b) F–HAp, (c) HAp<sub>600 °C</sub> and (d) HAp<sub>900 °C</sub>.

Conversely, roots from the F–HAp and HAp<sub>600 °C</sub> samples exhibited more significant branching (laterally) with respect to the blank sample (water), thereby displaying superior root development [146]. Enhanced root growth is likely to be related to metabolic acceleration due to the supply of phosphorus and cobalt nutrients by F–HAp and HAp<sub>600 °C</sub>.

#### 4. Conclusions

The present work investigated different “low-cost/low-end” hydroxyapatite-based adsorbents obtained from Amazon Tambaqui fish cleaning residues. The effect of the annealing temperature on atrazine herbicide and cobalt ions adsorption was explored. Bare fish bone residues mainly comprised of biogenic carbonated hydroxyapatite turned out to be able to adsorb low concentration of atrazine (initial concentration equal to 10 mg L<sup>-1</sup>) by relying on Van der Waals interaction and hydrogen bonds sensibly ascribed to collagen moieties. With atrazine traces removal being a “grand challenge” of current wastewater treatment technologies, pristine hydroxyapatite could be exploited as a “zero-cost” material suitable for atrazine complete removal after conventional biological/mechanical

cleaning processes. Nonetheless, the “saturation” of collagen sites and steric hindrance effects cranked down the atrazine adsorption on pristine hydroxyapatite at higher pesticide concentrations; however, heat-treated (600 and 900 °C) samples were able to adsorb larger amounts of atrazine according to the surface dehydroxylation level. As for cobalt adsorption, thermally treated materials showed favorable adsorption isotherms (probably due to ion exchange) and reflected inner pores availability to  $\text{Co}^{2+}$ . Cobalt and phosphate release tests were also performed in order to evaluate the applicability of the adsorbents as micro and macro nutrient carriers for agriculture in a slightly acidic medium-emulating standard fertilizer formulation. Pristine and 600 °C-annealed samples could liberate phosphate concentrations equal to or greater than  $2 \text{ mg L}^{-1}$  by virtue of structural defects favoring the material solubilization. On the other hand,  $\text{Co}^{2+}$  desorption was deeply affected by the different affinity for cobalt of the three hydroxyapatite-based materials. In fact, pristine hydroxyapatite and the material treated at 900 °C released between 20 and  $30 \text{ mg L}^{-1}$  of  $\text{Co}^{2+}$  because of adsorption mechanism involving only the external part of the material. Furthermore, the cytotoxic assay pointed out the importance of mineral supply, suggesting the beneficial effects in terms of seed germination and root elongation due to  $\text{Co}^{2+}$  and  $\text{PO}_4^{3-}$  release from pristine fish bone residues and mildly heat-treated hydroxyapatite. Consistently with circular economic principles, worthless fishery waste was used as a functional “zero-cost” material amenable to combined use as adsorbent for different industry dealing with heavy metal (e.g., mining, electronics, electroplating, etc.) and agrochemical disposal and as source of mineral nutrients for soil fertilization.

**Author Contributions:** Conceptualization, E.C.P.; Investigation, C.G.R. and T.M.d.O.R.; Methodology, C.G.R., T.M.d.O.R., J.O.D.M., C.S.S.A. and G.L.d.S.; Resources, E.C.P.; Supervision, B.A.M.F. and E.C.P.; Visualization, B.A.M.F.; Writing—original draft, C.G.R., T.M.d.O.R. and J.O.D.M.; Writing—review & editing, C.G.R., T.M.d.O.R., J.O.D.M., S.Q. and E.C.P. All authors have read and agreed to the published version of the manuscript.

**Funding:** This research was funded by EMBRAPA (grant number 11.14.03.001.01.00) and FAPESP (grant number 2021/14992-1). This study was financed in part by the Coordenação de Aperfeiçoamento de Pessoal de Nível Superior-Brasil (CAPES)-Finance Code 001.

**Data Availability Statement:** Not applicable.

**Acknowledgments:** The authors acknowledge EMBRAPA, FINEP, SisNano, and AgroNano Network for further support.

**Conflicts of Interest:** The authors declare no conflict of interest. The funders had no role in the design of the study; in the collection, analyses, or interpretation of data; in the writing of the manuscript; or in the decision to publish the results.

## References

1. Crutzen, P.J. Geology of Mankind—The Anthropocene. *Nature* **2002**, *415*, 23. [[CrossRef](#)] [[PubMed](#)]
2. Shen, J.; Huang, G.; An, C.; Xin, X.; Huang, C.; Rosendahl, S. Removal of Tetrabromobisphenol A by Adsorption on Pinecone-Derived Activated Charcoals: Synchrotron FTIR, Kinetics and Surface Functionality Analyses. *Bioresour. Technol.* **2018**, *247*, 812–820. [[CrossRef](#)] [[PubMed](#)]
3. Jawad, A.H.; Abdulhameed, A.S.; Mastuli, M.S. Mesoporous Crosslinked Chitosan-Activated Charcoal Composite for the Removal of Thionine Cationic Dye: Comprehensive Adsorption and Mechanism Study. *J. Polym. Environ.* **2020**, *28*, 1095–1105. [[CrossRef](#)]
4. Yadav, S.; Asthana, A.; Chakraborty, R.; Jain, B.; Singh, A.K.; Carabineiro, S.A.C.; Susan, M.A.B.H. Cationic Dye Removal Using Novel Magnetic/Activated Charcoal/ $\beta$ -Cyclodextrin/Alginate Polymer Nanocomposite. *Nanomaterials* **2020**, *10*, 170. [[CrossRef](#)] [[PubMed](#)]
5. Khandaker, S.; Chowdhury, M.F.; Awual, M.R.; Islam, A.; Kuba, T. Efficient Cesium Encapsulation from Contaminated Water by Cellulosic Biomass Based Activated Wood Charcoal. *Chemosphere* **2021**, *262*, 127801. [[CrossRef](#)]
6. Gar Alalm, M.; Nasr, M. Artificial Intelligence, Regression Model, and Cost Estimation for Removal of Chlorothalonil Pesticide by Activated Carbon Prepared from Casuarina Charcoal. *Sustain. Environ. Res.* **2018**, *28*, 101–110. [[CrossRef](#)]

7. Crini, G.; Lichtfouse, E.; Wilson, L.D.; Morin-Crini, N. Conventional and Non-Conventional Adsorbents for Wastewater Treatment. *Environ. Chem. Lett.* **2019**, *17*, 195–213. [[CrossRef](#)]
8. Wang, F.; Shih, K. Adsorption of Perfluorooctanesulfonate (PFOS) and Perfluorooctanoate (PFOA) on Alumina: Influence of Solution PH and Cations. *Water Res.* **2011**, *45*, 2925–2930. [[CrossRef](#)]
9. Dao, T.H.; Nguyen, N.T.; Nguyen, M.N.; Ngo, C.L.; Luong, N.H.; Le, D.B.; Pham, T.D. Adsorption Behavior of Polyelectrolyte onto Alumina and Application in Ciprofloxacin Removal. *Polymers* **2020**, *12*, 1554. [[CrossRef](#)]
10. Banerjee, S.; Dubey, S.; Gautam, R.K.; Chattopadhyaya, M.C.; Sharma, Y.C. Adsorption Characteristics of Alumina Nanoparticles for the Removal of Hazardous Dye, Orange G from Aqueous Solutions. *Arab. J. Chem.* **2019**, *12*, 5339–5354. [[CrossRef](#)]
11. Tabesh, S.; Davar, F.; Loghman-Estarki, M.R. Preparation of  $\gamma$ -Al<sub>2</sub>O<sub>3</sub> Nanoparticles Using Modified Sol-Gel Method and Its Use for the Adsorption of Lead and Cadmium Ions. *J. Alloys Compd.* **2018**, *730*, 441–449. [[CrossRef](#)]
12. Momina; Shahadat, M.; Isamil, S. Regeneration Performance of Clay-Based Adsorbents for the Removal of Industrial Dyes: A Review. *RSC Adv.* **2018**, *8*, 24571–24587. [[CrossRef](#)]
13. Liu, P.; Zhang, L. Adsorption of Dyes from Aqueous Solutions or Suspensions with Clay Nano-Adsorbents. *Sep. Purif. Technol.* **2007**, *58*, 32–39. [[CrossRef](#)]
14. Zhang, T.; Wang, W.; Zhao, Y.; Bai, H.; Wen, T.; Kang, S.; Song, G.; Song, S.; Komarneni, S. Removal of Heavy Metals and Dyes by Clay-Based Adsorbents: From Natural Clays to 1D and 2D Nano-Composites. *Chem. Eng. J.* **2021**, *420*, 127574. [[CrossRef](#)]
15. Leenheer, J.A. Comprehensive Approach to Preparative Isolation and Fractionation of Dissolved Organic Carbon from Natural Waters and Wastewaters. *Environ. Sci. Technol.* **1981**, *15*, 578–587. [[CrossRef](#)]
16. Hochuli, E.; Döbeli, H.; Schacher, A. New Metal Chelate Adsorbent Selective for Proteins and Peptides Containing Neighbouring Histidine Residues. *J. Chromatogr. A* **1987**, *411*, 177–184. [[CrossRef](#)]
17. Alexandre, M.; Dubois, P. Polymer-Layered Silicate Nanocomposites: Preparation, Properties and Uses of a New Class of Materials. *Mater. Sci. Eng. R Rep.* **2000**, *28*, 1–63. [[CrossRef](#)]
18. Lebaron, P.C.; Wang, Z.; Pinnavaia, T.J. Polymer-Layered Silicate Nanocomposites: An Overview. *Appl. Clay Sci.* **1999**, *15*, 11–29. [[CrossRef](#)]
19. Hong, M.; Yu, L.; Wang, Y.; Zhang, J.; Chen, Z.; Dong, L.; Zan, Q.; Li, R. Heavy Metal Adsorption with Zeolites: The Role of Hierarchical Pore Architecture. *Chem. Eng. J.* **2019**, *359*, 363–372. [[CrossRef](#)]
20. Huang, Y.; Zeng, X.; Guo, L.; Lan, J.; Zhang, L.; Cao, D. Heavy Metal Ion Removal of Wastewater by Zeolite-Imidazolate Frameworks. *Sep. Purif. Technol.* **2018**, *194*, 462–469. [[CrossRef](#)]
21. Aljerf, L. High-Efficiency Extraction of Bromocresol Purple Dye and Heavy Metals as Chromium from Industrial Effluent by Adsorption onto a Modified Surface of Zeolite: Kinetics and Equilibrium Study. *J. Environ. Manag.* **2018**, *225*, 120–132. [[CrossRef](#)] [[PubMed](#)]
22. Jiang, N.; Shang, R.; Heijman, S.G.J.; Rietveld, L.C. High-Silica Zeolites for Adsorption of Organic Micro-Pollutants in Water Treatment: A Review. *Water Res.* **2018**, *144*, 145–161. [[CrossRef](#)] [[PubMed](#)]
23. Kobielska, P.A.; Howarth, A.J.; Farha, O.K.; Nayak, S. Metal–Organic Frameworks for Heavy Metal Removal from Water. *Coord. Chem. Rev.* **2018**, *358*, 92–107. [[CrossRef](#)]
24. Li, J.; Wang, X.; Zhao, G.; Chen, C.; Chai, Z.; Alsaedi, A.; Hayat, T.; Wang, X. Metal-Organic Framework-Based Materials: Superior Adsorbents for the Capture of Toxic and Radioactive Metal Ions. *Chem. Soc. Rev.* **2018**, *47*, 2322–2356. [[CrossRef](#)] [[PubMed](#)]
25. Khan, M.S.; Shahid, M. *Improving Water Quality Using Metal–Organic Frameworks*; American Chemical Society: Washington, DC, USA, 2021; pp. 171–191.
26. Shahnawaz Khan, M.; Khalid, M.; Shahid, M. What Triggers Dye Adsorption by Metal Organic Frameworks? The Current Perspectives. *Mater. Adv.* **2020**, *1*, 1575–1601. [[CrossRef](#)]
27. Yan, J.W.; Wu, J.; Lu, L.; Wang, J.; Guo, J.; Sakiyama, H.; Muddassir, M.; Khan, M.S. Photocatalytic Performances and Mechanisms of Two Coordination Polymers Based on Rigid Tricarboxylate. *J. Solid State Chem.* **2022**, *316*, 123602. [[CrossRef](#)]
28. Gupta, A.; Thakur, I.S. Treatment of Organic Recalcitrant Contaminants in Wastewater. In *Biological Wastewater Treatment and Resource Recovery*; Books on Demand: Norderstedt, Germany, 2017; pp. 3–16. [[CrossRef](#)]
29. Joseph, L.; Jun, B.M.; Flora, J.R.V.; Park, C.M.; Yoon, Y. Removal of Heavy Metals from Water Sources in the Developing World Using Low-Cost Materials: A Review. *Chemosphere* **2019**, *229*, 142–159. [[CrossRef](#)]
30. Ali, I.; Gupta, V.K. Advances in Water Treatment by Adsorption Technology. *Nat. Protoc.* **2007**, *1*, 2661–2667. [[CrossRef](#)]
31. Klementová, Š.; Hornychová, L.; Šorf, M.; Zemanová, J.; Kahoun, D. Toxicity of Atrazine and the Products of Its Homogeneous Photocatalytic Degradation on the Aquatic Organisms Lemna Minor and Daphnia Magna. *Environ. Sci. Pollut. Res.* **2019**, *26*, 27259–27267. [[CrossRef](#)]
32. Moreira, A.J.; Pinheiro, B.S.; Araújo, A.F.; Freschi, G.P.G. Evaluation of Atrazine Degradation Applied to Different Energy Systems. *Environ. Sci. Pollut. Res.* **2016**, *23*, 18502–18511. [[CrossRef](#)]
33. Nayak, A.; Bhushan, B. Hydroxyapatite as an Advanced Adsorbent for Removal of Heavy Metal Ions from Water: Focus on Its Applications and Limitations. *Mater. Today Proc.* **2021**, *46*, 11029–11034. [[CrossRef](#)]

34. Mohd Pu'ad, N.A.S.; Koshy, P.; Abdullah, H.Z.; Idris, M.I.; Lee, T.C. Syntheses of Hydroxyapatite from Natural Sources. *Heliyon* **2019**, *5*, e01588. [[CrossRef](#)]
35. Kongsri, S.; Janpradit, K.; Buapa, K.; Techawongstien, S.; Chanthai, S. Nanocrystalline Hydroxyapatite from Fish Scale Waste: Preparation, Characterization and Application for Selenium Adsorption in Aqueous Solution. *Chem. Eng. J.* **2013**, *215–216*, 522–532. [[CrossRef](#)]
36. Pai, S.; M Kini, S.; Selvaraj, R.; Pugazhendhi, A. A Review on the Synthesis of Hydroxyapatite, Its Composites and Adsorptive Removal of Pollutants from Wastewater. *J. Water Process Eng.* **2020**, *38*, 101574. [[CrossRef](#)]
37. Amenaghawon, A.N.; Anyalewechi, C.L.; Darmokoesoemo, H.; Kusuma, H.S. Hydroxyapatite-Based Adsorbents: Applications in Sequestering Heavy Metals and Dyes. *J. Environ. Manag.* **2022**, *302*, 113989. [[CrossRef](#)]
38. Sharma, P.; Rohilla, D.; Chaudhary, S.; Kumar, R.; Singh, A.N. Nanosorbent of Hydroxyapatite for Atrazine: A New Approach for Combating Agricultural Runoffs. *Sci. Total Environ.* **2019**, *653*, 264–273. [[CrossRef](#)]
39. Milošević, D.; Lević, S.; Lazarević, S.; Veličković, Z.; Marinković, A.; Petrović, R.; Petrović, P. Hybrid Material Based on Subgleba of Mosaic Puffball Mushroom (*Handkea utrififormis*) as an Adsorbent for Heavy Metal Removal from Aqueous Solutions. *J. Environ. Manag.* **2021**, *297*, 113358. [[CrossRef](#)]
40. Hokkanen, S.; Bhatnagar, A.; Srivastava, V.; Suorsa, V.; Sillanpää, M. Removal of Cd<sup>2+</sup>, Ni<sup>2+</sup> and PO<sub>4</sub><sup>3-</sup> from Aqueous Solution by Hydroxyapatite-Bentonite Clay-Nanocellulose Composite. *Int. J. Biol. Macromol.* **2018**, *118*, 903–912. [[CrossRef](#)]
41. Chu, Y.; Xia, M.; Wang, F.; Yan, X.; Dai, Y.; Dong, L.; Zhang, Y. The Uptake Performance and Microscopic Mechanism of Inorganic-Organic Phosphorus Hybrid Amorphous Hydroxyapatite for Multiple Heavy Metal Ions. *Colloids Surf. A Physicochem. Eng. Asp.* **2022**, *640*, 128384. [[CrossRef](#)]
42. Pon-On, W.; Suntornsaratoon, P.; Charoenphandhu, N.; Thongbunchoo, J.; Krishnamra, N.; Tang, I.M. Hydroxyapatite from Fish Scale for Potential Use as Bone Scaffold or Regenerative Material. *Mater. Sci. Eng. C* **2016**, *62*, 183–189. [[CrossRef](#)]
43. Rustad, T. Turid Rustad Utilization of Marine By-Product. *Electron. J. Environ. Agric. Food Chem.* **2003**, *2*, 458–463.
44. Kong, L.; Liu, X.; Lv, G.; Liu, T.; Zhang, P.; Li, Y.; Chen, B.; Liao, L. Copper Adsorption Using Hydroxyapatite Derived from Bovine Bone. *Adv. Civ. Eng.* **2022**, *2022*, 1026129. [[CrossRef](#)]
45. Meski, S.; Tazibt, N.; Khireddine, H.; Ziani, S.; Biba, W.; Yala, S.; Sidane, D.; Boudjouan, F.; Moussaoui, N. Synthesis of Hydroxyapatite from Mussel Shells for Effective Adsorption of Aqueous Cd(II). *Water Sci. Technol.* **2019**, *80*, 1226–1237. [[CrossRef](#)]
46. Alshahrani, A.A.; Alorabi, A.Q.; Hassan, M.S.; Amna, T.; Azizi, M. Chitosan-Functionalized Hydroxyapatite-Cerium Oxide Heterostructure: An Efficient Adsorbent for Dyes Removal and Antimicrobial Agent. *Nanomaterials* **2022**, *12*, 2713. [[CrossRef](#)]
47. Li, S.; Wang, J.; Jing, X.; Liu, Q.; Saba, J.; Mann, T.; Zhang, M.; Wei, H.; Chen, R.; Liu, L. Conversion of Calcined Eggshells into Flower-like Hydroxyapatite Agglomerates by Solvothermal Method Using Hydrogen Peroxide/N,N-Dimethylformamide Mixed Solvents. *J. Am. Ceram. Soc.* **2012**, *95*, 3377–3379. [[CrossRef](#)]
48. Liu, Y.; Nadeem, A.; Sebastian, S.; Olsson, M.A.; Wai, S.N.; Styring, E.; Engellau, J.; Isaksson, H.; Tägil, M.; Lidgren, L.; et al. Bone Mineral: A Trojan Horse for Bone Cancers. Efficient Mitochondria Targeted Delivery and Tumor Eradication with Nano Hydroxyapatite Containing Doxorubicin. *Mater. Today Bio* **2022**, *14*, 100227. [[CrossRef](#)]
49. FAO. *The State of World Fisheries and Aquaculture*; 190AD; FAO: Rome, Italy, 2020; Volume 5, ISBN 9781424464968.
50. Islam, J.M.; Yap, E.E.S.; Krongpong, L.; Toppe, J.; Peñarubia, O.R. *Fish Waste Management an Assesement of the Potential Production and Utilisation of Fish Silage in Bangladesh, Phillipines and Thailand*; FAO: Rome, Italy, 2021; Volume 1216, ISBN 9789251340790.
51. Guillen, J.; Natale, F.; Carvalho, N.; Casey, J.; Hofherr, J.; Druon, J.N.; Fiore, G.; Gibin, M.; Zanzi, A.; Martinsohn, J.T. Global Seafood Consumption Footprint. *Ambio* **2019**, *48*, 111–122. [[CrossRef](#)]
52. Fortes Carvalho Neta, R.N.; Pinheiro Sousa, D.B.; de Macêdo Sobrinho, I.C.; Yarbrough Horton, E.; da Silva de Almeida, Z.; Tchaicka, L.; de Sousa, A.L. Genotoxic and Hematological Parameters in *Colossoma macropomum* (Pisces, Serrasalminidae) as Biomarkers for Environmental Impact Assessment in a Protected Area in Northeastern Brazil. *Environ. Sci. Pollut. Res.* **2015**, *22*, 15994–16003. [[CrossRef](#)] [[PubMed](#)]
53. Goulding, M.; Carvalho, M.L. Life History and Management of the Tambaqui (*Colossoma Macropomum*, Characidae): An Important Amazonian Food Fish. *Rev. Bras. Zool.* **1982**, *1*, 107–133. [[CrossRef](#)]
54. Associação Brasileira de Piscicultura. *Anuário 2022 PeixeBR da Piscicultura 2022*; Associação Brasileira de Piscicultura: Brasília, Brazil, 2022; p. 1.
55. Valenti, W.C.; Barros, H.P.; Moraes-Valenti, P.; Bueno, G.W.; Cavalli, R.O. Aquaculture in Brazil: Past, Present and Future. *Aquac. Rep.* **2021**, *19*, 100611. [[CrossRef](#)]
56. Damien, A.; Isabelle, T.; Christovam, B.; Nicolas, J.; Vincent, D. Land Use Sustainability on the South-Eastern Amazon Agricultural Frontier: Recent Progress and the Challenges Ahead. *Appl. Geogr.* **2017**, *80*, 86–97. [[CrossRef](#)]
57. Instituto Nacional Do Meio Ambiente e Dos Recursos Naturais (IBAMA). *Relatórios de Comercialização de Agrotóxicos*; Instituto Nacional Do Meio Ambiente e Dos Recursos Naturais (IBAMA): Brasília, Brazil, 2021.
58. Cruz, R.H.R.; Farias, A.L.d.A. Socio-Environmental Impacts of Oil Palm Production in the Paraense Amazon: Use of Agrochemicals. *Rev. Geoamazônia* **2017**, *5*, 86–109.



59. Castello, L.; Mcgrath, D.G.; Hess, L.L.; Coe, M.T.; Lefebvre, P.A.; Petry, P.; Macedo, M.N.; Renó, V.F.; Arantes, C.C. The Vulnerability of Amazon Freshwater Ecosystems. *Conserv. Lett.* **2013**, *6*, 217–229. [[CrossRef](#)]
60. Ferri, M.; Campisi, S.; Polito, L.; Shen, J.; Gervasini, A. Tuning the Sorption Ability of Hydroxyapatite/Carbon Composites for the Simultaneous Remediation of Wastewaters Containing Organic-Inorganic Pollutants. *J. Hazard. Mater.* **2021**, *420*, 126656. [[CrossRef](#)]
61. Pignatti, W.A.; e Lima, F.A.N.d.S.; de Lara, S.S.; Correa, M.L.M.; Barbosa, J.R.; Leão, L.H.D.C.; Pignatti, M.G. Spatial Distribution of Pesticide Use in Brazil: A Strategy for Health Surveillance. *Cienc. Saude Coletiva* **2017**, *22*, 3281–3293. [[CrossRef](#)]
62. Siqueira, G.W.; Pereira, S.D.F.P.; Aprile, F.M. Determination of Trace Elements (Zn, Co and Ni) in Sediments at the Amazon Continental Shelf on Influence of the Amazon River Discharge. *Acta Amaz.* **2006**, *36*, 321–326. [[CrossRef](#)]
63. Sass, J.B.; Colangelo, A. European Union Bans Atrazine, While the United States Negotiates Continued Use. *Int. J. Occup. Environ. Health* **2006**, *12*, 260–267. [[CrossRef](#)]
64. Barceloux, D.G.; Barceloux, D. Cobalt. *J. Toxicol. Clin. Toxicol.* **1999**, *37*, 201–216. [[CrossRef](#)]
65. Azevedo-Santos, V.M.; Rodrigues-Filho, J.L.; Fearnside, P.M.; Lovejoy, T.E.; Brito, M.F.G. Conservation of Brazilian Freshwater Biodiversity: Thinking about the next 10 Years and Beyond. *Biodivers. Conserv.* **2021**, *30*, 235–241. [[CrossRef](#)]
66. Thomaz, S.M.; Gomes Barbosa, L.; de Souza Duarte, M.C.; Panosso, R. Opinion: The Future of Nature Conservation in Brazil. *Inland Waters* **2020**, *10*, 295–303. [[CrossRef](#)]
67. Graymore, M.; Stagnitti, F.; Allinson, G. Impacts of Atrazine in Aquatic Ecosystems. *Environ. Int.* **2001**, *26*, 483–495. [[CrossRef](#)]
68. Brovini, E.M.; de Deus, B.C.T.; Vilas-Boas, J.A.; Quadra, G.R.; Carvalho, L.; Mendonça, R.F.; Pereira, R.d.O.; Cardoso, S.J. Three-Bestseller Pesticides in Brazil: Freshwater Concentrations and Potential Environmental Risks. *Sci. Total Environ.* **2021**, *771*, 144754. [[CrossRef](#)]
69. Atrazine, O.; National, E.P.A.; List, P.; States, U.; States, U.; Rico, P. Draft Toxicological Profile for Atrazine. In *ATSDR's Toxicological Profiles*; Agency for Toxic Substances and Disease Registry: Atlanta, GA, USA, 2002; pp. 129–160. [[CrossRef](#)]
70. Leyssens, L.; Vinck, B.; Van Der Straeten, C.; Wuyts, F.; Maes, L. Cobalt Toxicity in Humans—A Review of the Potential Sources and Systemic Health Effects. *Toxicology* **2017**, *387*, 43–56. [[CrossRef](#)]
71. Hansen, E.; Nilsson, N.H.; Lithner, D.; Lassen, C. *Hazardous Substances in Plastic Materials*; COWI A/S: Kongens Lyngby, Denmark, 2013; Volume 148.
72. Ministério de Estado Da Agricultura, Pecuária e Abastecimento (MAPA). *Instrução Normativa n. 46 de 22/11/2016*. 72; Ministério de Estado Da Agricultura, Pecuária e Abastecimento (MAPA): Brasília, Brazil, 2016.
73. Cryosystems, O. Crystallographica Search-Match. *J. Appl. Cryst.* **1999**, *32*, 379–380. [[CrossRef](#)]
74. Holland, T.J.B.; Redfern, S.A.T. Unit Cell Refinement from Powder Diffraction Data: The Use of Regression Diagnostics. *Miner. Mag.* **1997**, *61*, 65–77. [[CrossRef](#)]
75. Momma, K.; Izumi, F. VESTA 3 for Three-Dimensional Visualization of Crystal, Volumetric and Morphology Data. *J. Appl. Cryst.* **2011**, *44*, 1272–1276. [[CrossRef](#)]
76. Lagergren, S. About the Theory of So-Called Adsorption of Soluble Substances. *K. Sven. Vetenskapsakademiens. Handlingar. Band* **1898**, *24*, 1–39.
77. Ho, Y.S.; McKay, G. Pseudo-Second Order Model for Sorption Processes. *Process Biochem.* **1999**, *34*, 451–465. [[CrossRef](#)]
78. Vargas, A.M.M.; Cazetta, A.L.; Kunita, M.H.; Silva, T.L.; Almeida, V.C. Adsorption of Methylene Blue on Activated Carbon Produced from Flamboyant Pods (Delonix Regia): Study of Adsorption Isotherms and Kinetic Models. *Chem. Eng. J.* **2011**, *168*, 722–730. [[CrossRef](#)]
79. Langmuir, I. The Constitution and Fundamental Properties of Solids and Liquids. II. Liquids. *J. Am. Chem. Soc.* **1917**, *39*, 1848–1906. [[CrossRef](#)]
80. Freundlich, H.M.F. Uber Die Adsorption in Losungen. *J. Phys. Chem.* **1906**, *57*, 385–470. [[CrossRef](#)]
81. Murphy, J.; Riley, J.P. A Modified Single Solution Method for the Determination of Phosphate in Natural Waters. *Anal. Chim. Acta* **1962**, *27*, 31–36. [[CrossRef](#)]
82. Crouch, S.R.; Malmstadt, H.V. A Mechanistic Investigation of Molybdenum Blue Method for Determination of Phosphate. *Anal. Chem.* **1967**, *39*, 1405. [[CrossRef](#)]
83. Hanrahan, G.; Salmassi, T.M.; Khachikian, C.S.; Foster, K.L. Reduced Inorganic Phosphorus in the Natural Environment: Significance, Speciation and Determination. *Talanta* **2005**, *66*, 435–444. [[CrossRef](#)] [[PubMed](#)]
84. McLaughlin, M.J.; McBeath, T.M.; Smernik, R.; Stacey, S.P.; Ajiboye, B.; Guppy, C. The Chemical Nature of P Accumulation in Agricultural Soils—Implications for Fertiliser Management and Design: An Australian Perspective. *Plant Soil* **2011**, *349*, 69–87. [[CrossRef](#)]
85. Hodge, H.C.; Lefevre, M.L.; Bale, W.F. Chemical and X-ray Diffraction Studies of Calcium Phosphates. *Ind. Eng. Chem. Anal. Ed.* **1938**, *10*, 156–161. [[CrossRef](#)]
86. Kay, M.I.; Young, R.A.; Posner, A.S. Crystal Structure of Hydroxyapatite. *Nature* **1964**, *204*, 1050–1052. [[CrossRef](#)]
87. Palache, C.; Berman, H.; Frondel, C. *Dana's System of Mineralogy*, 7th ed.; Wiley: Hoboken, NJ, USA, 1952; Volume 74.
88. Visser, J.W.; de Wolff, P.M. Absolute Intensities—Report 641.109. Technisch Physische Dienst: Delft, The Netherlands, 1964.
89. Bano, N.; Jikan, S.S.; Basri, H.; Adzila, S.; Zago, D.M. XRD and FTIR Study of A&B Type Carbonated Hydroxyapatite Extracted from Bovine Bone. *AIP Conf. Proc.* **2019**, *2068*, 020100.



90. Londoño-Restrepo, S.M.; Millán-Malo, B.M.; del Real-López, A.; Rodríguez-García, M.E. In Situ Study of Hydroxyapatite from Cattle during a Controlled Calcination Process Using HT-XRD. *Mater. Sci. Eng. C* **2019**, *105*, 110020. [\[CrossRef\]](#)
91. McElderry, J.D.P.; Zhu, P.; Mroue, K.H.; Xu, J.; Pavan, B.; Fang, M.; Zhao, G.; McNerny, E.; Kohn, D.H.; Franceschi, R.T.; et al. Crystallinity and Compositional Changes in Carbonated Apatites: Evidence from <sup>31</sup>P Solid-State NMR, Raman, and AFM Analysis. *J. Solid State Chem.* **2013**, *206*, 192–198. [\[CrossRef\]](#)
92. Fleet, M.E. Infrared Spectra of Carbonate Apatites: N2-Region Bands. *Biomaterials* **2009**, *30*, 1473–1481. [\[CrossRef\]](#)
93. Tonegawa, T.; Ikoma, T.; Yoshioka, T.; Hanagata, N.; Tanaka, J. Crystal Structure Refinement of A-Type Carbonate Apatite by X-Ray Powder Diffraction. *J. Mater. Sci.* **2010**, *45*, 2419–2426. [\[CrossRef\]](#)
94. Talal, A.; Hamid, S.K.; Khan, M.; Khan, A.S. Structure of Biological Apatite. In *Handbook of Ionic Substituted Hydroxyapatites*; Elsevier: Amsterdam, The Netherlands, 2020; pp. 1–19.
95. Zubieta-Otero, L.F.; Londoño-Restrepo, S.M.; Lopez-Chavez, G.; Hernandez-Becerra, E.; Rodríguez-García, M.E. Comparative Study of Physicochemical Properties of Bio-Hydroxyapatite with Commercial Samples. *Mater. Chem. Phys.* **2021**, *259*, 124201. [\[CrossRef\]](#)
96. Shaltout, A.A.; Allam, M.A.; Moharram, M.A. FTIR Spectroscopic, Thermal and XRD Characterization of Hydroxyapatite from New Natural Sources. *Spectrochim. Acta A Mol. Biomol. Spectrosc.* **2011**, *83*, 56–60. [\[CrossRef\]](#)
97. Degirmenbasi, N.; Kalyon, D.M.; Birinci, E. Biocomposites of Nanohydroxyapatite with Collagen and Poly(Vinyl Alcohol). *Colloids Surf. B Biointerfaces* **2006**, *48*, 42–49. [\[CrossRef\]](#)
98. Payne, K.J.; Veis, A. Fourier Transform Ir Spectroscopy of Collagen and Gelatin Solutions: Deconvolution of the Amide I Band for Conformational Studies. *Biopolymers* **1988**, *27*, 1749–1760. [\[CrossRef\]](#)
99. Tavakol, S.; Nikpour, M.R.; Amani, A.; Soltani, M.; Rabiee, S.M.; Rezayat, S.M.; Chen, P.; Jahanshahi, M. Bone Regeneration Based on Nano-Hydroxyapatite and Hydroxyapatite/Chitosan Nanocomposites: An In Vitro and In Vivo Comparative Study. *J. Nanopart. Res.* **2013**, *15*, 1373. [\[CrossRef\]](#)
100. Muhammad, N.; Gao, Y.; Iqbal, F.; Ahmad, P.; Ge, R.; Nishan, U.; Rahim, A.; Gonfa, G.; Ullah, Z. Extraction of Biocompatible Hydroxyapatite from Fish Scales Using Novel Approach of Ionic Liquid Pretreatment. *Sep. Purif. Technol.* **2016**, *161*, 129–135. [\[CrossRef\]](#)
101. Drouet, C. Apatite Formation: Why It May Not Work as Planned, and How to Conclusively Identify Apatite Compounds. *BioMed Res. Int.* **2013**, *2013*, 490946. [\[CrossRef\]](#)
102. Samanta, A.; Chanda, D.K.; Das, P.S.; Ghosh, J.; Mukhopadhyay, A.K.; Dey, A. Synthesis of Nano Calcium Hydroxide in Aqueous Medium. *J. Am. Ceram. Soc.* **2016**, *99*, 787–795. [\[CrossRef\]](#)
103. Snavey, D.L.; Dubsky, J. Near-IR Spectra of Polyethylene, Polyethylene Glycol, and Polyvinylethyl Ether. *J. Polym. Sci. A Polym. Chem.* **1996**, *34*, 2575–2579. [\[CrossRef\]](#)
104. Hooi, M.T.; Phang, S.W.; Yow, H.Y.; David, E.; Kim, N.X.; Choo, H.L. FTIR Spectroscopy Characterization and Critical Comparison of Poly(Vinyl)Alcohol and Natural Hydroxyapatite Derived from Fish Bone Composite for Bone-Scaffold. *J. Phys. Conf. Ser.* **2021**, *2120*, 012004. [\[CrossRef\]](#)
105. Goloshchapov, D.L.; Lenshin, A.S.; Savchenko, D.V.; Seredin, P.V. Importance of Defect Nanocrystalline Calcium Hydroxyapatite Characteristics for Developing the Dental Biomimetic Composites. *Results Phys.* **2019**, *13*, 102158. [\[CrossRef\]](#)
106. Rey, C.; Marsan, O.; Combes, C.; Drouet, C.; Grossin, D.; Sarda, S. Characterization of Calcium Phosphates Using Vibrational Spectroscopies. *Adv. Calcium Phosphate Biomater.* **2014**, *2*, 229–266.
107. Rehman, I.; Bonfield, W. Characterization of Hydroxyapatite and Carbonated Apatite by Photo Acoustic FTIR Spectroscopy. *J. Mater. Sci. Mater. Med.* **1997**, *8*, 1–4. [\[CrossRef\]](#)
108. Zhou, W.Y.; Wang, M.; Cheung, W.L.; Guo, B.C.; Jia, D.M. Synthesis of Carbonated Hydroxyapatite Nanospheres through Nanoemulsion. *J. Mater. Sci. Mater. Med.* **2008**, *19*, 103–110. [\[CrossRef\]](#)
109. Youness, R.A.; Taha, M.A.; Elhaes, H.; Ibrahim, M. Molecular Modeling, FTIR Spectral Characterization and Mechanical Properties of Carbonated-Hydroxyapatite Prepared by Mechanochemical Synthesis. *Mater. Chem. Phys.* **2017**, *190*, 209–218. [\[CrossRef\]](#)
110. Israelachvili, J. *Intermolecular and Surface Forces*; Academic Press: Cambridge, MA, USA, 2011.
111. Porsani, N.K.; Trombini, V.; Ana, P.A.; Setz, L.F.G. Rheological Evaluation of Hydroxyapatite. *Ceramica* **2018**, *64*, 325–330. [\[CrossRef\]](#)
112. Yoganand, C.P.; Selvarajan, V.; Goudouri, O.M.; Paraskevopoulos, K.M.; Wu, J.; Xue, D. Preparation of Bovine Hydroxyapatite by Transferred Arc Plasma. *Curr. Appl. Phys.* **2011**, *11*, 702–709. [\[CrossRef\]](#)
113. Ivanova, T.I.; Frank-Kamenetskaya, O.V.; Kol'tsov, A.B.; Ugolkov, V.L. Crystal Structure of Calcium-Deficient Carbonated Hydroxyapatite. Thermal Decomposition. *J. Solid State Chem.* **2001**, *160*, 340–349. [\[CrossRef\]](#)
114. Wilson, R.M.; Elliott, J.C.; Dowker, S.E.P.; Rodríguez-Lorenzo, L.M. Rietveld Refinements and Spectroscopic Studies of the Structure of Ca-Deficient Apatite. *Biomaterials* **2005**, *26*, 1317–1327. [\[CrossRef\]](#)
115. Zyman, Z.Z.; Rokhmistrov, D.V.; Glushko, V.I.; Ivanov, I.G. Thermal Impurity Reactions and Structural Changes in Slightly Carbonated Hydroxyapatite. *J. Mater. Sci. Mater. Med.* **2009**, *20*, 1389–1399. [\[CrossRef\]](#)
116. Elliott, J.C. Structure and Chemistry of the Apatites and Other Calcium Orthophosphates. In *Studies in Organic Chemistry*; Elsevier: Amsterdam, The Netherlands, 1994; Volume 18.

117. Ramirez-Gutierrez, C.F.; Londoño-Restrepo, S.M.; del Real, A.; Mondragón, M.A.; Rodríguez-García, M.E. Effect of the Temperature and Sintering Time on the Thermal, Structural, Morphological, and Vibrational Properties of Hydroxyapatite Derived from Pig Bone. *Ceram. Int.* **2017**, *43*, 7552–7559. [[CrossRef](#)]
118. Lozano, L.F.; Peña-Rico, M.A.; Jang-Cho, H.; Heredia, A.; Villareal, E.; Ocotlán-Flores, J.; Gomez-Cortes, A.L.; Aranda-Manteca, F.J.; Orozco, E.; Bucio, L. Thermal Properties of Mineralized and Non Mineralized Type I Collagen in Bone. *Mater. Res. Soc. Symp. Proc.* **2002**, *724*, N7.6. [[CrossRef](#)]
119. Tõnsuaadu, K.; Gross, K.A.; Pluduma, L.; Veiderma, M. A Review on the Thermal Stability of Calcium Apatites. *J. Therm. Anal. Calorim.* **2012**, *110*, 647–659. [[CrossRef](#)]
120. Ramanathan, G.; Singaravelu, S.; Raja, M.D.; Liji Sobhana, S.S.; Sivagnanam, U.T. Extraction and Characterization of Collagen from the Skin of Arothron Stellatus Fish—A Novel Source of Collagen for Tissue Engineering. *J. Biomater. Tissue Eng.* **2014**, *4*, 203–209. [[CrossRef](#)]
121. Liao, C.J.; Lin, F.H.; Chen, K.S.; Sun, J.S. Thermal Decomposition and Reconstitution of Hydroxyapatite in Air Atmosphere. *Biomaterials* **1999**, *20*, 1807–1813. [[CrossRef](#)]
122. Wang, T.; Dorner-Reisel, A.; Müller, E. Thermogravimetric and Thermokinetic Investigation of the Dehydroxylation of a Hydroxyapatite Powder. *J. Eur. Ceram. Soc.* **2004**, *24*, 693–698. [[CrossRef](#)]
123. Wang, P.E.; Chaki, T.K. Sintering Behaviour and Mechanical Properties of Hydroxyapatite and Dicalcium Phosphate. *J. Mater. Sci. Mater. Med.* **1993**, *4*, 150–158. [[CrossRef](#)]
124. Li, Y.; Kong, F.; Weng, W. Preparation and Characterization of Novel Biphasic Calcium Phosphate Powders ( $\alpha$ -TCP/HA) Derived from Carbonated Amorphous Calcium Phosphates. *J. Biomed. Mater. Res. B Appl. Biomater.* **2009**, *89*, 508–517. [[CrossRef](#)]
125. Astala, R.; Stott, M.J. First Principles Investigation of Mineral Component of Bone:  $\text{CO}_3$  Substitutions in Hydroxyapatite. *Chem. Mater.* **2005**, *17*, 4125–4133. [[CrossRef](#)]
126. Bonfield, W.; Gibson, I.R. Novel Synthesis and Characterization of an AB-Type Carbonate-Substituted Hydroxyapatite. *J. Biomed. Mater. Res.* **2002**, *59*, 697–708. [[CrossRef](#)]
127. Trombe, J.C.; Montel, G. Some Features of the Incorporation of Oxygen in Different Oxidation States in the Apatitic Lattice—I On the Existence of Calcium and Strontium Oxyapatites. *J. Inorg. Nucl. Chem.* **1978**, *40*, 15–21. [[CrossRef](#)]
128. Cihlář, J.; Buchal, A.; Trunec, M. Kinetics of Thermal Decomposition of Hydroxyapatite Bioceramics. *J. Mater. Sci.* **1999**, *34*, 6121–6131. [[CrossRef](#)]
129. Park, H.C.; Baek, D.J.; Park, Y.M.; Yoon, S.Y.; Stevens, R. Thermal Stability of Hydroxyapatite Whiskers Derived from the Hydrolysis of  $\alpha$ -TCP. *J. Mater. Sci.* **2004**, *39*, 2531–2534. [[CrossRef](#)]
130. Jaworski, J.W.; Cho, S.; Kim, Y.; Jung, J.H.; Jeon, H.S.; Min, B.K.; Kwon, K.Y. Hydroxyapatite Supported Cobalt Catalysts for Hydrogen Generation. *J. Colloid Interface Sci.* **2013**, *394*, 401–408. [[CrossRef](#)]
131. Kramer, E.; Itzkowitz, E.; Wei, M. Synthesis and Characterization of Cobalt-Substituted Hydroxyapatite Powders. *Ceram. Int.* **2014**, *40*, 13471–13480. [[CrossRef](#)]
132. Handley-Sidhu, S.; Renshaw, J.C.; Moriyama, S.; Stolpe, B.; Mennan, C.; Bagheriasl, S.; Yong, P.; Stamboulis, A.; Paterson-Beedle, M.; Sasaki, K.; et al. Uptake of  $\text{Sr}^{2+}$  and  $\text{Co}^{2+}$  into Biogenic Hydroxyapatite: Implications for Biomineral Ion Exchange Synthesis. *Environ. Sci. Technol.* **2011**, *45*, 6985–6990. [[CrossRef](#)]
133. Pang, Y.; Kong, L.; Chen, D.; Yuvaraja, G.; Mehmood, S. Facile Synthesis of Cobalt Doped Hydroxyapatite as Hydroxyl Promoted Peroxymonosulfate Activator for Degradation of Rhodamine B. *J. Hazard. Mater.* **2020**, *384*, 121447. [[CrossRef](#)]
134. Pyo, E.; Lee, K.; Jang, M.J.; Ko, I.H.; Kim, C.S.; Choi, S.M.; Lee, S.; Kwon, K.Y. Cobalt Incorporated Hydroxyapatite Catalyst for Water Oxidation. *ChemCatChem* **2019**, *11*, 5425–5429. [[CrossRef](#)]
135. McCabe, W.L.; Smith, J.C.; Harriott, P. *Unit Operations of Chemical Engineering*, 4th ed.; McGraw-Hill: New York, NY, USA, 1985.
136. Foo, K.Y.; Hameed, B.H. Insights into the Modeling of Adsorption Isotherm Systems. *Chem. Eng. J.* **2010**, *156*, 2–10. [[CrossRef](#)]
137. Langmuir, I. The Constitution and Fundamental Properties of Solids and Liquids. Part I. Solids. *J. Am. Chem. Soc.* **1916**, *38*, 5425–5429. [[CrossRef](#)]
138. Al-Ghouti, M.A.; Da'ana, D.A. Guidelines for the Use and Interpretation of Adsorption Isotherm Models: A Review. *J. Hazard. Mater.* **2020**, *393*, 122383. [[CrossRef](#)]
139. Ferri, M.; Campisi, S.; Gervasini, A. Nickel and Cobalt Adsorption on Hydroxyapatite: A Study for the de-Metalation of Electronic Industrial Wastewaters. *Adsorption* **2019**, *25*, 649–660. [[CrossRef](#)]
140. Handley-Sidhu, S.; Mullan, T.K.; Grail, Q.; Albadarneh, M.; Ohnuki, T.; MacAskie, L.E. Influence of PH, Competing Ions, and Salinity on the Sorption of Strontium and Cobalt onto Biogenic Hydroxyapatite. *Sci. Rep.* **2016**, *6*, 23361. [[CrossRef](#)]
141. Handley-Sidhu, S.; Renshaw, J.C.; Yong, P.; Kerley, R.; Macaskie, L.E. Nano-Crystalline Hydroxyapatite Bio-Mineral for the Treatment of Strontium from Aqueous Solutions. *Biotechnol. Lett.* **2011**, *33*, 79–87. [[CrossRef](#)]
142. Handley-Sidhu, S.; Hriljac, J.A.; Cuthbert, M.O.; Renshaw, J.C.; Patrick, R.A.D.; Charnock, J.M.; Stolpe, B.; Lead, J.R.; Baker, S.; Macaskie, L.E. Bacterially Produced Calcium Phosphate Nanobiominerals: Sorption Capacity, Site Preferences, and Stability of Captured Radionuclides. *Environ. Sci. Technol.* **2014**, *48*, 6891–6898. [[CrossRef](#)]
143. Sciena, C.R.; dos Santos, M.F.; Moreira, F.K.V.; Sena Neto, A.R.; Marconcini, J.M.; Correa, D.S.; Paris, E.C. Starch:Pectin Acidic Sachets Development for Hydroxyapatite Nanoparticles Storage to Improve Phosphorus Release. *J. Polym. Environ.* **2019**, *27*, 794–802. [[CrossRef](#)]

144. Hankermeyer, C.R.; Ohashi, K.L.; Delaney, D.C.; Ross, J.; Constantz, B.R. Dissolution Rates of Carbonated Hydroxyapatite in Hydrochloric Acid. *Biomaterials* **2002**, *23*, 743–750. [[CrossRef](#)]
145. Wang, D.; Xie, Y.; Jaisi, D.P.; Jin, Y. Effects of Low-Molecular-Weight Organic Acids on the Dissolution of Hydroxyapatite Nanoparticles. *Environ. Sci. Nano* **2016**, *3*, 768–779. [[CrossRef](#)]
146. Malafatti, J.O.D.; Moreira, A.J.; Sciena, C.R.; Silva, T.E.M.; Freschi, G.P.G.; Pereira, E.C.; Paris, E.C. Prozac<sup>®</sup> Removal Promoted by HAP:Nb<sub>2</sub>O<sub>5</sub>nanoparticles System: By-Products, Mechanism, and Cytotoxicity Assessment. *J. Environ. Chem. Eng.* **2021**, *9*, 104820. [[CrossRef](#)]

**Disclaimer/Publisher's Note:** The statements, opinions and data contained in all publications are solely those of the individual author(s) and contributor(s) and not of MDPI and/or the editor(s). MDPI and/or the editor(s) disclaim responsibility for any injury to people or property resulting from any ideas, methods, instructions or products referred to in the content.